



2 Synchronization of tubular pressure oscillations in interacting 3 nephrons

4 O.V. Sosnovtseva ^{a,b,*}, D.E. Postnov ^a, E. Mosekilde ^b, N.-H. Holstein-Rathlou ^c

5 ^a Department of Physics, Saratov State University, Astrakhanskaya str. 83, Saratov 410026, Russia

6 ^b Department of Physics, The Technical University of Denmark, 2800 Kgs. Lyngby, Denmark

7 ^c Department of Medical Physiology, Panum Institute, University of Copenhagen, 2200 Copenhagen N, Denmark

8 Abstract

9 ■■■. © 2002 Elsevier Science Ltd. All rights reserved.

11 1. Introduction

12 By controlling the excretion of water and salts, the kidneys play an important role in regulating the blood pressure
13 and maintaining a proper environment for the cells of the body. This control depends to large extent on mechanisms
14 that are associated with the individual functional unit, the nephron. However, a variety of cooperative phenomena
15 arising through interactions among the nephrons may also be important. The purpose of this paper is to present ex-
16 perimental evidence for a coupling between nephrons that are connected through a common piece of afferent blood
17 vessel, to develop a mathematical model that can account for the observed synchronization phenomena, and to discuss
18 the possible physiological significance of these phenomena. We shall be particularly interested in the synchronization
19 effects that can occur among neighboring nephrons that individually display irregular (or chaotic) dynamics in their
20 pressure and flow regulation.

21 It has long been recognized that the ability of the nephrons to compensate for variations in the arterial blood
22 pressure primarily rests with the so-called tubuloglomerular feedback (TGF) by which the nephron can regulate the
23 incoming blood flow in dependence of the ionic composition of the fluid leaving the loop of Henle [1]. Early experiments
24 by Leyssac and Baumbach [2] and by Leyssac and Holstein-Rathlou [3,4] demonstrated that this feedback regulation
25 can become unstable and generate self-sustained oscillations in the proximal intratubular pressure with a typical period
26 of 30–40 s. With different amplitudes and phases the same oscillations have also been observed in the distal intratubular
27 pressure and in the chloride concentration near the terminal part of the loop of Henle [5]. While for normal rats the
28 oscillations have the appearance of a limit cycle with a sharply peaked power spectrum reflecting the period of the cycle,
29 highly irregular oscillations, displaying a broadband spectral distribution with significant subharmonic components,
30 were observed for spontaneously hypertensive rats (SHR) [3].

31 It has subsequently been demonstrated [6,7] that irregular oscillations can occur for normal rats as well, provided
32 that the arterial blood pressure is increased by ligating the blood flow to the other kidney (so-called 2 kidney-1 clip
33 Goldblatt hypertension). In a particular experiment, where the function of the nephron was accidentally disturbed,
34 evidence of a period-doubling transition was observed [8]. Together with the above mentioned subharmonic compo-
35 nents in the spectral distribution for the hypertensive rats, this type of qualitative change in behavior provides evidence

* Corresponding author. Address: Department of Physics, Saratov State University, Astrakhanskaya str. 83, Saratov 410026, Russia.

E-mail address: olga@fysik.dtu.dk (O.V. Sosnovtseva).

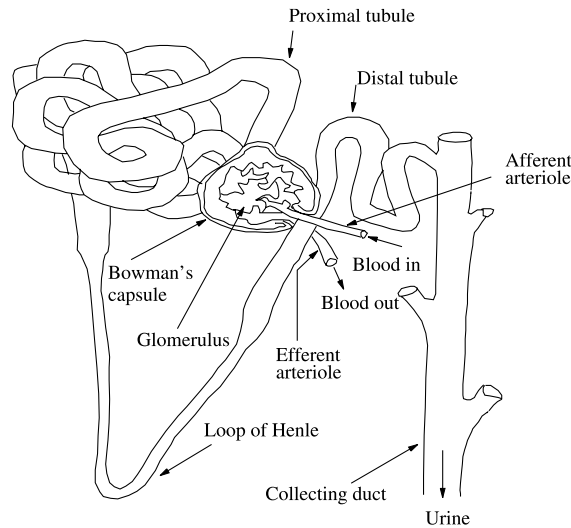


Fig. 1. Sketch of the main structural components of the nephron. Note particularly how the terminal part of the loop of Henle passes within cellular distances of the afferent arteriole, allowing the TGF mechanism to control the incoming blood flow in response to the ionic composition of the fluid leaving the loop of Henle. Reproduced from a Master Thesis by M.D. Andersen and N. Carlsson.

36 in support of the hypothesis that the pressure and flow regulation in the rat nephron operates close to a transition to
37 deterministic chaos [9,10].

38 As illustrated in the schematic drawing of Fig. 1, the TGF regulation is made possible by the interesting anatomical
39 feature that the terminal part of the ascending limb of the loop of Henle passes within cellular distances of the afferent
40 arteriole for the same nephron. At the point of contact, specialized cells (the macula densa cells) monitor the NaCl
41 concentration of the tubular fluid and produce a signal that activates the smooth muscle cells in the arteriolar wall. The
42 higher the glomerular filtration is, the faster the fluid will flow through the loop of Henle, and the higher the NaCl
43 concentration will be at the macula densa cells. A high NaCl concentration causes the macula densa cells to activate the
44 vascular smooth muscle cells in the arteriolar wall and thus to reduce the diameter of that vessel. Hence, the blood flow
45 and thereby the glomerular filtration are lowered, and the TGF mechanism operates as a negative feedback system.

46 The steady state response of the arteriolar flow regulation can be obtained from open-loop experiments [11] in which
47 a paraffin block is inserted into the middle of the proximal tubule and the rate of filtration is measured as a function of
48 an externally forced flow of artificial tubular fluid into the loop of Henle. Reflecting physiological constraints on the
49 diameter of the arteriole, this response follows an S-shaped characteristic with a maximum at low Henle flows and a
50 lower saturation level at externally forced flows beyond 20–25 nl/min. The steepness of the response is significantly
51 higher for SHR than for normotensive rats [12]. Together with the delay in the TGF regulation, this steepness plays an
52 essential role for the stability of the feedback system [5,13], and the experimentally observed higher steepness for SHR
53 may therefore explain the more complicated pressure variations observed in these rats.

54 A main component in the regulatory delay is associated with the finite transit time of the fluid through the tubular
55 system. The length of this delay can be estimated from the phase shift between the pressure oscillations in the proximal
56 tubule and the oscillations of the NaCl concentration in the distal tubule. A typical value is 10–15 s [14]. In addition
57 there is a transmission time of 3–5 s for the signal from the macula densa cells to reach the smooth muscle cells in the
58 arteriolar wall [5,14]. In total this delay is sufficient for the nephrons in normotensive rats to operate close to or slightly
59 beyond a Hopf bifurcation [13,15]. There is evidence to show that similar oscillations occur in man [16].

60 Besides reacting to the TGF signal, the afferent arteriole also responds to variations in the pressure difference across
61 the arteriolar wall. This response consists of a passive elastic component in parallel with an active muscular (or myo-
62 genic) component. A similar response appears to be involved in the autoregulation of the blood flow to many other
63 organs, and the significance of this element in the nephron pressure and flow regulation is clearly revealed in experi-
64 ments where the spectral response to a noise input is determined [17]. Here, one observes a peak at frequencies con-
65 siderably higher than the frequencies of the TGF regulation and corresponding to typical arteriolar dynamics. Based on
66 in vitro experiments on the strain–stress relationship for muscle strips, Feldberg et al. [18] have proposed a mathe-

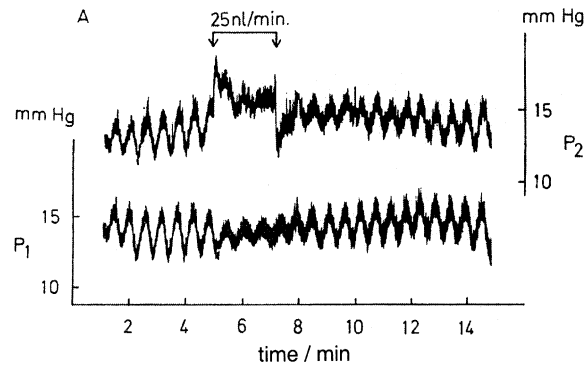


Fig. 2. Results of a microperfusion experiment for a pair of neighboring nephrons. Arrows indicate the start and stop of the perfusion phase. In the microperfused nephron (top trace), the tubular pressure oscillations are blocked during the perfusion. During the same period, the amplitude of the oscillations are reduced in the nonperfused nephron (lower trace).

67 matical model for the reaction of the arteriolar wall in the individual nephron. This model plays an essential role in our
68 description of the pressure and flow regulation for the nephron.

69 However, the functional units do not operate independently of one another. The nephrons are typically arranged in
70 couples or triplets with their afferent arterioles branching off from a common interlobular artery (or cortical radial
71 artery) [19], and this proximity allows them to interact in various ways. Experimental results by Holstein-Rathlou [20]
72 show how neighboring nephrons tend to adjust their TGF-mediated pressure oscillations so as to attain a state of in-
73 phase synchronization. Holstein-Rathlou has also demonstrated how microperfusion with artificial tubular fluid in one
74 nephron affects the amplitude of the pressure variations in a neighboring nephron, allowing the magnitude of the
75 nephron-nephron interaction to be estimated [20].

76 As an illustration of these results, Fig. 2 shows how microperfusion into the proximal tubule of one nephron can
77 influence the pressure oscillations in a neighboring nephron. In the microperfused nephron (top trace) the proximal
78 tubular pressure oscillations are blocked during the microperfusion. Arrows indicate the start and stop of the perfusion
79 phase. During the same period, the amplitude of the oscillations is decreased in the nonperfused nephron (lower trace).
80 Note how the oscillations are reactivated simultaneously in both nephrons, and how the in-phase synchronization
81 between the nephrons is reestablished after a few minutes. This type of cross-talk among the nephrons is assumed to be
82 produced by signals that are transmitted along the afferent arterioles [20]. The mechanisms underlying such a coupling
83 are not known in detail. However, two different types of interaction seem plausible,

84 (i) A coupling between the TGF mechanisms of neighboring nephrons. The presence of such an interaction is well-
85 established experimentally, but the underlying cellular mechanisms remain less understood. It is likely that the coupling
86 is associated with a vascular propagated response where electrical signals, initiated by the TGF of one nephron, travel
87 across the smooth muscle cells in the arteriolar wall from the region close to the macula densa and upstream along the
88 arteriole to the branching point with the arteriole from the neighboring nephron. Because of the relatively high speed at
89 which such signals propagate as compared with the length of the vessels and the period of the TGF-mediated oscil-
90 lations, this type of coupling tends to produce in-phase synchronization. If the afferent arteriole of one nephron is
91 stimulated by the TGF-mechanism to contract, the vascular signals almost immediately reach the neighboring nephron
92 and cause it to contract as well.

93 (ii) A much simpler type of coupling that we shall refer to as hemodynamic coupling. This coupling arises from the
94 fact that if one nephron is stimulated by its TGF-mechanism to contract its afferent arteriole, then the hydrostatic
95 pressure rises over the neighboring nephron, and the blood flow to this nephron increases. Half a period later when the
96 increased blood flow activates the TGF-mechanism in the neighboring nephron and causes its afferent arteriole to
97 contract, the blood flow to this nephron is again reduced, and the blood flow to the first nephron increases. This type of
98 coupling tends to produce out-of-phase or anti-phase synchronization between the pressure oscillations of the two
99 nephrons. In reality, we expect both mechanisms to be present simultaneously. Depending on the precise structure of
100 the arteriolar network this may cause one mechanism to be the more important for the local coupling of closely situated
101 nephrons, while the other mechanism might be important for more global coupling phenomena. It is worth noting that
102 simulation results for systems of interacting nephrons were published already by Jensen et al. [8] and by Bohr et al. [21].
103 These studies describe a variety of different synchronization patterns including a chess-board pattern of anti-phase
104 synchronization for nephrons arranged in a square lattice. However, at the time when these studies were performed the

105 physiological mechanisms underlying the nephron–nephron interaction were not yet understood. The present discussion
106 of interacting nephrons is based on our recent publications [22–25].

107 2. Single-nephron model

108 Our model of the individual nephron [22] considers the proximal tubule as an elastic structure with little or no flow
109 resistance [10,22]. The pressure P_t in the proximal tubule changes in response to differences between the in- and out-
110 going fluid flows

$$\frac{dP_t}{dt} = \frac{1}{C_{\text{tub}}} [F_{\text{filt}} - F_{\text{reab}} - F_{\text{Hen}}]. \quad (1)$$

112 Here F_{filt} is the glomerular filtration rate, F_{reab} represents the reabsorption that takes place in the proximal tubule, F_{Hen}
113 is the flow of fluid into the loop of Henle, and C_{tub} is the elastic compliance of the tubule. The Henle flow,

$$F_{\text{Hen}} = \frac{P_t - P_d}{R_{\text{Hen}}}, \quad (2)$$

115 is determined by the difference between the proximal (P_t) and the distal (P_d) tubular pressures and by the flow resistance
116 R_{Hen} . This description is clearly a simplification, since a significant reabsorption of water and salts occurs during
117 passage of the loop of Henle. However, within the physiologically relevant flow range it provides a good approximation
118 to the experimentally determined pressure-flow relation [9].

119 As the filtrate flows into the descending limb of the loop of Henle, the NaCl concentration in the fluid surrounding
120 the tubule increases significantly, and osmotic processes cause water to be reabsorbed. At the same time, salts and
121 metabolic byproducts are secreted into the tubular fluid. In the ascending limb, on the other hand, the tubular wall is
122 nearly impermeable to water. Here, the epithelial cells contain molecular pumps that transport sodium and chloride
123 from the tubular fluid into the space between the nephrons (the interstitium). These processes are accounted for in
124 considerable detail in the spatially extended model developed by Holstein-Rathlou et al. [13]. In the present model, the
125 reabsorption F_{reab} in the proximal tubule and the flow resistance R_{Hen} are treated as constants.

126 The glomerular filtration rate is given by [26]

$$F_{\text{filt}} = (1 - H_a) \left(1 - \frac{C_a}{C_e}\right) \frac{P_a - P_g}{R_a}, \quad (3)$$

128 where the afferent hematocrit H_a represents the fraction that the blood cells constitute of the total blood volume at the
129 entrance to the glomerular capillaries. C_a and C_e are the protein concentrations of the afferent and efferent blood
130 plasma, respectively, and R_a is the flow resistance of the afferent arteriole. $(P_a - P_g)/R_a$ determines the incoming blood
131 flow. Multiplied by $(1 - H_a)$ this gives the plasma flow. Finally, the factor $(1 - C_a/C_e)$ relates the filtration rate to the
132 change in protein concentration for the plasma remaining in the vessel.

133 The glomerular pressure P_g is determined by distributing the arterial to venous pressure drop between the afferent
134 and the efferent arteriolar resistances and the protein concentration C_e in the efferent blood is obtained from the as-
135 sumption that filtration equilibrium is established before the blood leaves the glomerular capillaries. This leads to an
136 expression of the form

$$C_e = \frac{1}{2b} \left[\sqrt{a^2 - 4b(P_t - P_g)} - a \right], \quad (4)$$

138 where a and b are parameters relating the colloid osmotic pressure to the protein concentration [27].

139 The glomerular feedback is described by a sigmoidal relation between the muscular activation ψ of the afferent
140 arteriole and the delayed Henle flow $3x_3/T$

$$\psi = \psi_{\text{max}} - \frac{\psi_{\text{max}} - \psi_{\text{min}}}{1 + \exp[\alpha(3x_3/TF_{\text{Hen}0} - S)]}. \quad (5)$$

142 This expression is based on empirical results for the variation of the glomerular filtration with the flow into the loop of
143 Henle as obtained in the above mentioned open-loop experiments [12]. In Eq. (5), ψ_{max} and ψ_{min} denote the maximum
144 and the minimum values of the muscular activation. α determines the slope of the feedback curve. We have already
145 indicated that this slope plays an important role for the stability of the pressure and flow regulation. In Section 3 we use

146 α as one of the main bifurcation parameters. S is the displacement of the curve along the normalized flow axis, and F_{Hen0}
147 is a normalization value for the Henle flow.

148 The delay in the TGF is taken into account by means of a chain of three first-order coupled differential equations,

$$\frac{dx_1}{dt} = F_{\text{Hen}} - \frac{3}{T}x_1, \quad (6)$$

$$\frac{dx_2}{dt} = \frac{3}{T}(x_1 - x_2), \quad (7)$$

$$\frac{dx_3}{dt} = \frac{3}{T}(x_2 - x_3), \quad (8)$$

152 with T being the total delay time. In this way the delay is represented as a smoothed process, with x_1 and x_2 being
153 intermediate variables in the delay chain and with $3x_3/T$ being the delayed value of F_{Hen} .

154 The afferent arteriole is divided into two serially coupled sections of which the first (representing a fraction β of the
155 total length) is assumed to have a constant flow (or hemodynamic) resistance, while the second (closer to the glom-
156 erulus) is capable of varying its diameter and hence the flow resistance in dependence of the TGF activation,

$$R_a = R_{a0}[\beta + (1 - \beta)r^{-4}]. \quad (9)$$

158 Here, R_{a0} denotes a normal value of the arteriolar resistance and r is the radius of the active part of the vessel, nor-
159 malized relatively to its resting value. The hemodynamic resistance of the active part is assumed to vary inversely
160 proportional to r^4 . This is an application of Poiseuille's law for laminar flows.

161 Experiments have shown that arterioles tend to perform damped, oscillatory contractions in response to external
162 stimuli [28]. This behavior may be captured by the set of two coupled first-order differential equations

$$\frac{dv_r}{dt} + kv_r - \frac{P_{\text{av}} - P_{\text{eq}}}{\omega} = 0, \quad \frac{dr}{dt} = v_r. \quad (10)$$

164 Here, k is a characteristic time constant describing the damping of the arteriolar dynamics, and ω is a parameter that
165 controls the natural frequency of the oscillations. P_{av} is the average pressure in the active part of the arteriole, and P_{eq}
166 is the value of this pressure for which the arteriole is in equilibrium with its present radius at the existing muscular ac-
167 tivation.

168 As previously noted, the reaction of the arteriolar wall to changes in the blood pressure consists of a passive, elastic
169 component in parallel with an active, muscular response. The elastic component is determined by the properties of the
170 connective tissue. The active component in the strain–stress relation appears to be surprisingly simple. For some value
171 ϵ_{max} of the strain ϵ , the active stress attains a maximum, and on both sides the stress decreases almost linearly with
172 $|\epsilon - \epsilon_{\text{max}}|$. Moreover, the stress is proportional to the muscle tone ψ . By numerically integrating the passive and active
173 contributions across the arteriolar wall, one can establish a relation among the equilibrium pressure P_{eq} , the normalized
174 radius r , and the activation level ψ [18]. Unfortunately, computation of this relation for every time step of the simu-
175 lation model is quite time consuming. To speed up the process we have used an approximation in the form of the
176 analytic expression [22]

$$P_{\text{eq}} = 2.4 \times e^{10(r-1.4)} + 1.6(r-1) + \psi \left(\frac{4.7}{1 + e^{13(0.4-r)}} + 7.2(r+0.9) \right), \quad (11)$$

178 where P_{eq} is expressed in kPa (1 kPa = 10^3 N/m² \cong 7.5 mmHg). The first two terms in (11) represent the pressure vs.
179 radius relation for the nonactivated arteriole. The terms proportional to ψ represent the active response. This is ap-
180 proximately given by a sigmoidal term superimposed onto a linear term. The activation from the TGF mechanism is
181 assumed to be determined by (5). The expression in (11) closely reproduces the prediction of the more complex, ex-
182 perimentally based relation [22].

183 The above equations complete our description of the single-nephron model. A more detailed account of the
184 physiological processes underlying the model may be found in Topics in Nonlinear Dynamics [10] and in the paper by
185 Barfred et al. [22]. In total we have six coupled ordinary differential equations, each representing an essential physi-
186 ological relation. Because of the need to numerically evaluate C_c in each integration step, the model cannot be brought
187 onto an explicit form. The parameters applied in the single-nephron model may be found in our previous publications
188 [10,22].

189 **3. Bifurcation structure of the single-nephron model**

190 Fig. 3 shows an example of a one-dimensional bifurcation diagram for the single nephron model obtained by varying
191 the slope α of the open-loop response characteristics (5) while keeping the other parameters constant. In particular, the
192 delay in the feedback regulation is assumed to be $T = 16$ s. The diagram was constructed by combining a so-called brute
193 force bifurcation diagram with a bifurcation diagram obtained by means of continuation methods [30,31]. Such
194 methods allow us follow stable as well as unstable periodic orbits for a nonlinear dynamical system under variation of a
195 parameter and to identify the various bifurcations that the orbits undergo. Hence, in Fig. 3 fully drawn curves represent
196 stable solutions and dotted curves represent unstable periodic solutions.

197 For a given value of α , the brute force bifurcation diagram displays all the values of the relative arteriolar radius r
198 that the model attains when the steady state trajectory intersects a specified cross section in phase space. To reveal the
199 coexistence of several stable solutions, the brute force diagram has been obtained by scanning α in both directions.

200 For $T = 16$ s, the single nephron model undergoes a supercritical Hopf bifurcation at $\alpha \cong 11$ (outside the figure). In
201 this bifurcation, the equilibrium point loses its stability, and stable periodic oscillations emerge as the steady-state
202 solution. For $\alpha \cong 19.5$, at the point denoted PD_a^{1-2} in Fig. 3, the simple periodic oscillations undergo a period-doubling
203 bifurcation, and in a certain interval of α -values the period-2 cycle is the only stable solution. As we continue to increase
204 α , the period-2 solution undergoes a new period-doubling bifurcation at $\alpha \cong 22$ (i.e., at the point denoted PD_a^{2-4}). The
205 presence of a stable period-4 cycle is revealed in Fig. 3 by the fact that r assumes four different values for the same value
206 of α .

207 With further increase of α , the stable period-4 orbit undergoes two consecutive backwards period-doublings, so that
208 the original period-1 cycle again becomes stable around $\alpha = 26$. The stable period-1 cycle can hereafter be followed up
209 to $\alpha \cong 31$ where it is destabilized in a saddle-node bifurcation. The saddle cycle can be followed backwards in the
210 bifurcation diagram (dotted curve) to a point near $\alpha = 22.5$ where it undergoes a second saddle-node bifurcation, and a
211 new stable period-1 orbit is born. This cycle has a considerably larger amplitude than the original period-1 cycle. As the
212 parameter α is again increased, the new period-1 cycle undergoes a period-doubling cascade starting with the first
213 period-doubling bifurcation at $\alpha \cong 25$ and accumulating with the development of deterministic chaos near $\alpha = 27$. At
214 even higher values of α we notice the presence of a period-3 window near $\alpha = 28.5$ and the appearance of a stable
215 period-4 cycle around $\alpha = 33.5$.

216 The above scenario is typical of nonlinear dynamical systems when the amplitude of the internally generated os-
217 cillations becomes sufficiently large. In the bifurcation diagram of Fig. 3 this occurs when the slope of the feedback
218 characteristics exceeds a critical value. However, similar scenarios can be produced through variation of other pa-
219 rameters such as, for instance, the arterial pressure. This could explain the observation of chaos in normotensive rats
220 made hypertensive by clipping one of the renal arteries. On a qualitative level, the bifurcation diagram also agrees with
221 the experimental observation of a period-doubling in the response of a nephron to an external disturbance.

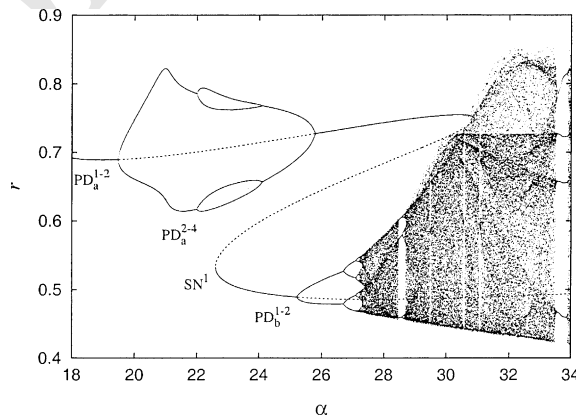


Fig. 3. One-dimensional bifurcation diagram for the single-nephron model obtained by varying the slope of the open-loop response characteristics. $T = 16$ s. Dotted curves represent unstable solutions determined by means of continuation techniques. Two saddle-node bifurcations of the period-1 cycle fold an uncompleted period-doubling structure over a complete period-doubling transition to chaos. Reproduced from a master thesis by M.D. Andersen and N. Carlsson.

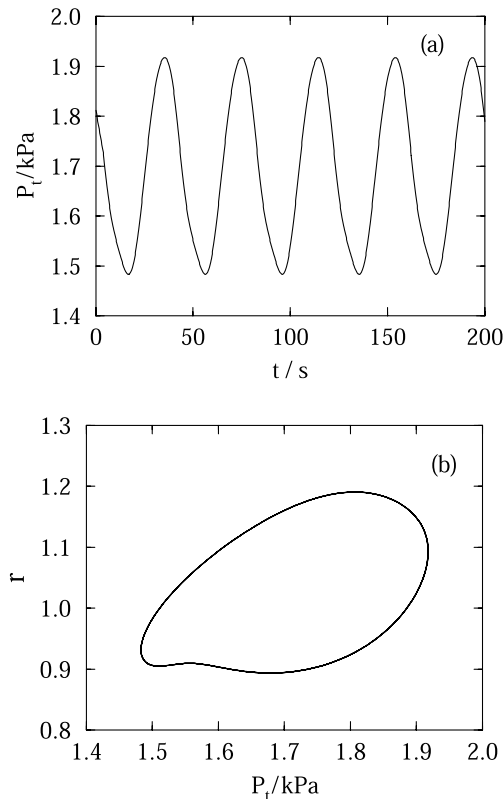


Fig. 4. (a) Temporal variation of the proximal tubular pressure P_t as obtained from the single-nephron model for $\alpha = 12$ and $T = 16$ s. (b) Corresponding phase plot. With the assumed parameters the model displays self-sustained oscillations in good agreement with the behavior observed for normotensive rats. The tubular pressure is given in kPa (1 kPa = 7.5 mmHg).

222 For normotensive rats, the typical operation point around $\alpha = 10$ – 12 and $T \cong 16$ s falls near the Hopf bifurcation
 223 point. This agrees with the finding that in a typical experiment about 70% of the nephrons perform self-sustained
 224 oscillations while the remaining show stable equilibrium behavior [5]. We can also imagine how the system is shifted
 225 back and forth across the Hopf bifurcation by variations in the arterial pressure. This explains the characteristic
 226 temporal behavior of the nephrons with periods of self-sustained oscillations interrupted by periods of stable equi-
 227 librium dynamics.

228 Fig. 4(a) shows the variation of the proximal tubular pressure P_t with time as calculated from the single nephron
 229 model for $\alpha = 12$ and $T = 16$ s. With these parameters the system operates slightly beyond the Hopf bifurcation point,
 230 and the depicted pressure variations represent the steady-state oscillations reached after the initial transient has died
 231 out. With physiologically realistic parameter values the model thus reproduces the observed self-sustained oscillations
 232 with appropriate periods and amplitudes. Fig. 4(b) shows the phase plot. Here, we have displayed the normalized
 233 arteriolar radius r against the proximal intratubular pressure. Again, the amplitude in the variations of r seems rea-
 234 sonable. Along the limit cycle the motion proceeds in the clockwise direction.

235 As previously noted, SHR have significantly larger α -values than normal rats ($\alpha = 16.8 \pm 12.0$ vs. $\alpha = 11.4 \pm 2.2$ for
 236 normotensive rats) [12]. On the other hand, it appears that the feedback delay is approximately the same for the two
 237 strains. Fig. 5(a) shows an example of the chaotic pressure variations obtained for higher values of the TGF response.
 238 Here, $\alpha = 32$ and $T = 16$ s. Under these conditions, the oscillations never repeat themselves and, as calculations show,
 239 the largest Lyapunov exponent is positive [32]. The corresponding phase plot in Fig. 5(b) displays the characteristic
 240 picture of a chaotic attractor. One can also analyse the behavior in terms of an interplay between the rapid modulations
 241 associated with the arteriolar dynamics and the slower TGF-mediated oscillations. The two modes never get into step
 242 with one-another, however. We shall return to a discussion of this mode interaction and its significance for the syn-
 243 chronization phenomena in Section 6.

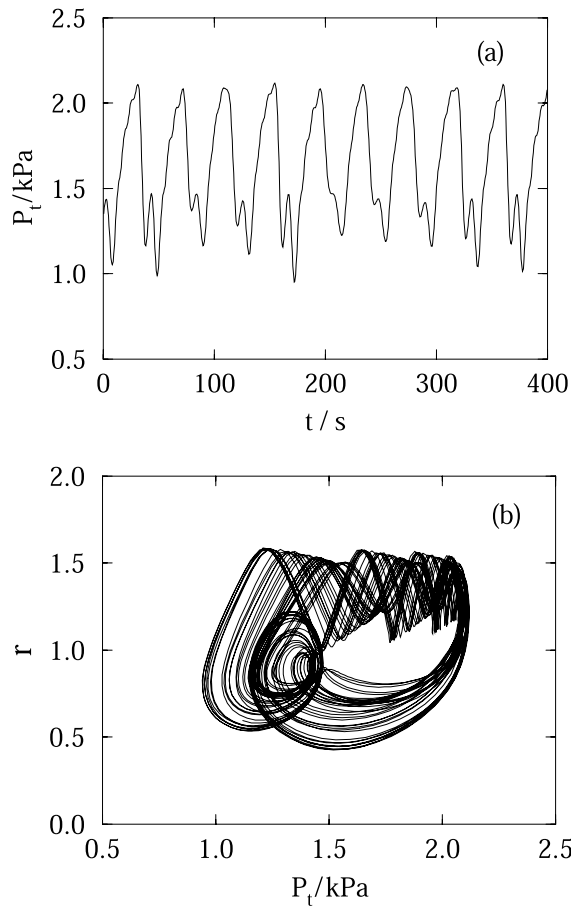


Fig. 5. (a) Pressure variations obtained from the single-nephron model for $\alpha = 32$ and $T = 16$ s. (b) Corresponding phase plot. With these parameters the model displays chaotic oscillations resembling the behavior observed for SHR [9].

244 4. Coupled nephrons

245 As illustrated in Fig. 6, the nephrons are typically arranged in pairs or triplets that share a common interlobular
 246 artery [19]. This anatomical feature allows neighboring nephrons to influence each others blood supply either through
 247 electrical signals that activate the vascular smooth muscle cells of the neighboring nephron or through a simple he-
 248 modynamic coupling. The two mechanisms depend very differently on the precise structure of the arteriolar network.
 249 Hence, variations of this structure may determine which of the mechanisms that is the more important. This could be of
 250 considerable biological interest, because the effects produced by the two mechanisms tend to be opposite in phase, and
 251 their influence on the overall behavior of the nephron system may be very different.

252 Let us start by considering the vascular coupling. The muscular activation ψ arises in the so-called juxtaglomerular
 253 apparatus and travels backwards along the afferent arteriole in a damped fashion. When it reaches the branching point
 254 with the arteriole from the neighboring nephron, it may propagate in the forward direction along that arteriole and
 255 start to contribute to its vascular response. In our model this type of cross-talk is represented by adding a contribution
 256 of the activation of one nephron to the activation of the other, i.e.,

$$\psi_{1,2\text{tot}} = \psi_{1,2} + \gamma\psi_{2,1} \quad (12)$$

258 where γ is the vascular coupling parameter, and ψ_1 and ψ_2 are the uncoupled activation levels of the two nephrons as
 259 determined by their respective Henle flows in accordance with Eq. (5).

260 As previously mentioned, the vascular signals propagate very fast as compared with the length of the vessels relative
 261 to the period of the TGF-oscillations. As a first approach, the vascular coupling can therefore be considered as in-

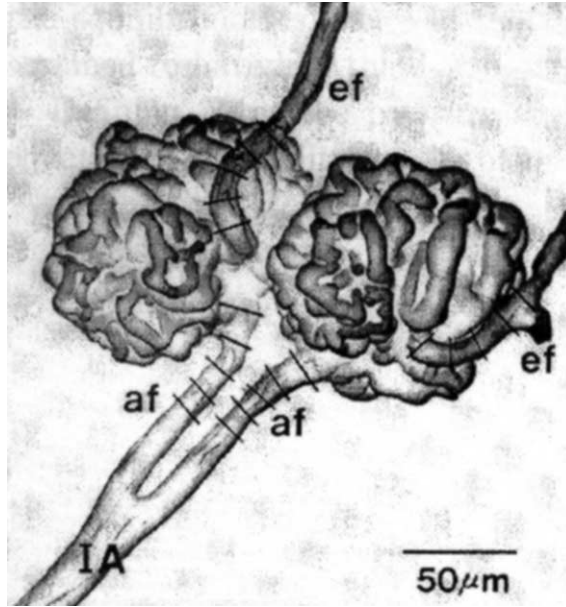


Fig. 6. Scanning electron microscope picture of the arteriolar system for a couple of adjacent nephrons. The nephrons are assumed to interact with one another via muscular contractions that propagate along the afferent arterioles (af) and via the so-called hemodynamic coupling.

262 stantaneous. Experimentally one observes [33] that the magnitude of the activation decreases exponentially as the signal
263 travels along a vessel. Hence, only a fraction of the activation from one nephron can contribute to the activation of the
264 neighboring nephron, and $\gamma = e^{-l/l_0} < 1$. Here, l is the propagation length for the coupling signal, and l_0 is the char-
265 acteristic length scale of the exponential decay. As a base case value, we shall use $\gamma = 0.2$.

266 To implement the hemodynamic coupling, a piece of common interlobular artery is included in the system, and the
267 total length of the incoming blood vessel is hereafter divided into a fraction $\varepsilon < \beta$ that is common to the two interacting
268 nephrons, a fraction $1 - \beta$ that is affected by the TGF signal, and a remaining fraction $\beta - \varepsilon$ for which the flow res-
269 istance is considered to remain constant. As compared with the equilibrium resistance of the separate arterioles, the
270 piece of shared artery is assumed to have half the flow resistance per unit length.

271 Defining P_ε as the pressure at the branching point of the two arterioles, the equation of continuity for the blood flow
272 reads

$$\frac{P_a - P_\varepsilon}{\varepsilon R_{a0}/2} = \frac{P_\varepsilon - P_{g1}}{R_{a1}} + \frac{P_\varepsilon - P_{g2}}{R_{a2}} \quad (13)$$

274 with

$$R_{a1} = (\beta - \varepsilon)R_{a0} + (1 - \beta)R_{a0}r_1^{-4} \quad (14)$$

276 and

$$R_{a2} = (\beta - \varepsilon)R_{a0} + (1 - \beta)R_{a0}r_2^{-4}. \quad (15)$$

278 Here, R_{a0} denotes the total flow resistance for each of the two arterioles in equilibrium. r_1 and r_2 are the normalized
279 radii of the active part of the afferent arterioles for nephron 1 and nephron 2, respectively, and P_{g1} and P_{g2} are the
280 corresponding glomerular pressures. As a base value of the hemodynamic coupling parameter we shall use $\varepsilon = 0.2$.

281 Because of the implicit manner in which the glomerular pressure is related to the efferent colloid osmotic pressure
282 and the filtration rate, direct solution of the set of seven coupled algebraic equations for the two-nephron system
283 becomes rather inefficient. Hence, for each nephron we have introduced the glomerular pressure P_g as a new state
284 variable determined by

$$\frac{dP_{g,i}}{dt} = \frac{1}{C_{glo}} \left(\frac{P_e - P_{g,i}}{R_{a,i}} - \frac{P_{g,i} - P_v}{R_e} - F_{filt,i} \right) \quad (16)$$

286 with $i = 1, 2$. This implies that we consider the glomerulus as an elastic structure with a compliance C_{glo} and with a
287 pressure variation determined by the imbalance between the incoming blood flow, the outgoing blood flow, and the
288 glomerular filtration rate.

289 From a physiological point of view, this formulation is well justified. Compared with the compliance of the proximal
290 tubule, C_{glo} is likely to be quite small, so that the model becomes numerically stiff. In the limit $C_{glo} \rightarrow 0$, the set of
291 differential equations reduces to the formulation with algebraic equations presented in Section 2. Finite values of C_{glo}
292 will change the damping of the system, and therefore also the details of the bifurcation structure. In practice, however,
293 the model will not be affected significantly as long as the time constant $C_{glo}R_{eff}$ is small compared with the periods of
294 interest. Here, R_{eff} denotes the effective flow resistance faced by C_{glo} .

295 Fig. 7 shows a phase plot for the steady-state behavior of one of the nephrons in the coupled nephron model. Here,
296 we have displayed the normalized radius of the active part of the afferent arteriole vs. the proximal tubular pressure for
297 $\gamma = \varepsilon = 0.2$. The two nephrons are assumed to have identical parameters, and with $T = 16$ s and $\alpha = 12$ the uncoupled
298 nephrons perform identical periodic motions with an arbitrary relation between their phases. Introduction of a coupling
299 forces the nephrons to synchronize their phases. Depending on the initial conditions and on the relative strength of the
300 two coupling mechanisms this synchronization may be either in phase or in anti-phase. The in-phase synchronization,
301 which produces a symmetric motion for the coupled system, is favored if the vascular coupling is relatively strong. Anti-
302 phase synchronization on the other hand, is more likely to occur in the presence of a strong hemodynamic coupling.

303 A typical example of anti-phase synchronization is demonstrated by the temporal variation of the tubular pressures
304 of the two periodically oscillating nephrons in Fig. 8. Here, $T = 16$ s, $\alpha = 12$, $\varepsilon = 0.3$ and $\gamma = 0.05$. With these pa-
305 rameters, the hemodynamic coupling dominates, and the nephrons operate precisely 180° out of phase.

306 The ability to synchronize is obviously not restricted to the case where the two nephrons are identical. In the
307 presence of a small parameter mismatch between the nephrons, a sufficiently strong coupling will again force the
308 nephrons to synchronize their pressure variations so that the periods become the same. In the nonlinear system each
309 nephron will adjust its pressure regulation relative to the other so as to attain a precise 1:1 relation between the periods.
310 This explains the experimental observation that many pairs of adjacent nephrons are found to exhibit precisely the same
311 period, even though they cannot be expected to have identical parameters [20]. As long as the mismatch is small, the
312 coupling strength required to synchronize the nephrons tend to scale in proportion with the size of the mismatch.

313 In the presence of a more significant parameter mismatch, the coupled nephrons will still tend to synchronize their
314 motions. However, in this case 1:1 synchronization may not be attainable, and instead the dynamics may be attracted to
315 a state where there is a rational relation ($n : m$ with n and m being integers) between the periods. For different degrees of
316 mismatch and different coupling strengths we expect to observe the full complexity of an Arnol'd tongue diagram with
317 its associated devil's staircase of frequency-locked regimes [34]. In the present case, however, the problem is further
318 complicated by the fact that the individual nephron involves two different modes. As discussed in Section 6, this allows
319 for the phenomenon of phase multistability.

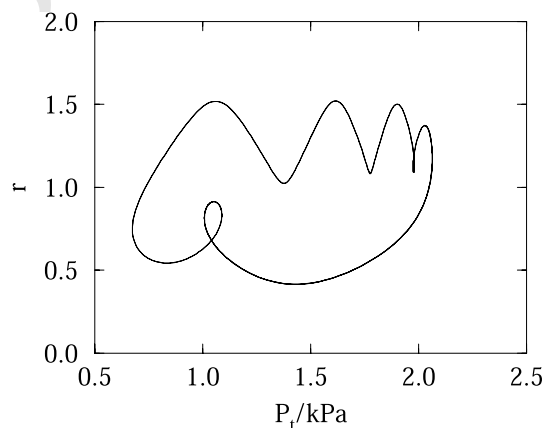


Fig. 7. Phase plot for the steady-state behavior of one of the nephrons in the coupled-nephron model. $\alpha = 12$, $T = 16$ s, $\varepsilon = \gamma = 0.2$. The two nephrons synchronize in phase and with a 1:5 synchronization between the two modes of the individual nephron.

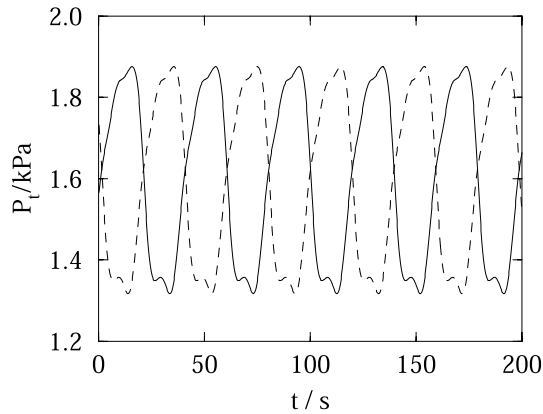


Fig. 8. Example of anti-phase synchronization in the temporal variation of the tubular pressures for two coupled periodically oscillating nephrons. $\alpha = 12$, $T = 16$ s, $\varepsilon = 0.3$, and $\gamma = 0.05$. With these parameters, the hemodynamic coupling dominates.

320 Let us hereafter examine the situation for larger values of α where the individual nephron exhibits chaotic dynamics.
321 Fig. 9(a) shows a phase plot for one of the nephrons in our two-nephron model for $\alpha = 32$, $T = 16$ s, $\varepsilon = 0.0$, and
322 $\gamma = 0.2$. Here we have introduced slight mismatch $\Delta T = 0.2$ s in the delay times between the two nephrons and, as

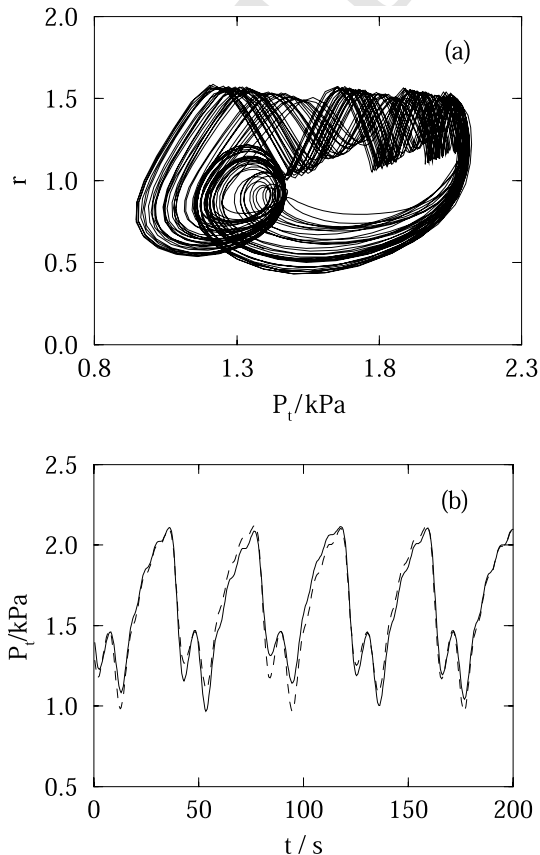


Fig. 9. (a) Phase plot for one of the nephrons, and (b) temporal variation of the tubular pressures for a pair of coupled chaotically oscillating nephrons ($\alpha = 32$, $T = 16$ s, and $\varepsilon = \gamma = 0.2$).

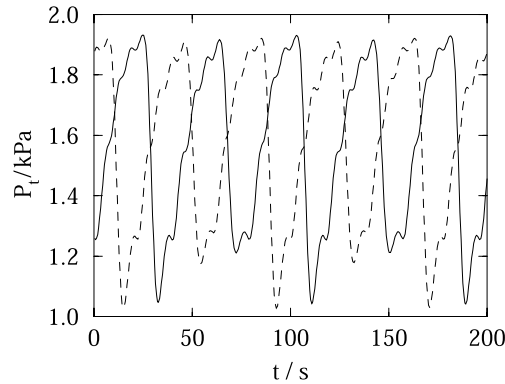


Fig. 10. Example of anti-phase synchronization of two chaotically oscillating nephrons ($\alpha = 32$, $T = 16$ s, $\varepsilon = 0.3$, and $\gamma = 0.05$).

323 illustrated by the tubular pressure variations of Fig. 9(b), the nephrons follow different trajectories. However, the
324 average period is precisely the same. This is a typical example of phase synchronization of two chaotic oscillators.

325 Let us finally consider a case where the hemodynamic coupling dominates the chaotic phase synchronization. Fig. 10
326 shows an example of the type of dynamics that one can observe in this situation. Here, $\alpha = 32$, $T = 16$ s, $\varepsilon = 0.3$, and
327 $\gamma = 0.05$. Each nephron is found to produce a chaotic variation in its tubular pressure. The nephrons have synchronized
328 their pressure variations with one another so that the average period is precisely the same, but the two nephrons clearly
329 operate in anti-phase with one another.

330 5. Experimental results

331 In order to study the interaction between the nephrons, experiments were performed with normotensive as well as
332 with SHR at the Department of Medical Physiology, University of Copenhagen, and the Department of Physiology,
333 Brown University [35].

334 During the experiments the rats were anesthetized, placed on a heated operating table to maintain the body tem-
335 perature, and connected to a small animal respirator to ensure a proper oxygen supply to the blood. The frequency of
336 the respirator was close to 1 Hz. This component is clearly visible in the frequency spectra of the observed tubular
337 pressure variations. Also observable is the frequency of the freely beating heart, which typically gives a contribution in
338 the 4–6 Hz regime. The frequencies involved in the nephron pressure and flow regulation are significantly lower and,
339 presumably, not influenced much by the respiratory and cardiac forcing signals [9].

340 When exposing the surface of a kidney, small glass pipettes, allowing simultaneous pressure measurements, could be
341 inserted into the proximal tubuli of a pair of adjacent, superficial nephrons. After the experiment, a vascular casting
342 technique was applied to determine if the considered nephron pair shared a common piece of afferent arteriole. Only
343 nephrons for which such a shared arteriolar segment was found showed clear evidence of synchronization, supporting
344 the hypothesis that the nephron–nephron interaction is mediated by the network of incoming blood vessels [19,36].

345 Fig. 11 shows an example of the tubular pressure variations that one can observe for adjacent nephrons of a
346 normotensive rat. For one of the nephrons, the pressure variations are drawn in black, and for the other nephron in
347 gray. Both curves show fairly regular variations in the tubular pressures with a period of approximately 31 s. The
348 amplitude is about 1.5 mm Hg and the mean pressure is close to 13 mm Hg. Inspection of the figure clearly reveals that
349 the oscillations are synchronized and remain nearly in phase for the entire observation period (corresponding to 25
350 periods of oscillation).

351 Fig. 12 shows an example of the opposite type of synchronization where the nephrons operate nearly 180° out of
352 phase. These results are also from a normotensive rat. As previously mentioned, we consider anti-phase synchronization
353 to be the signature of a strong hemodynamic component in the coupling, i.e., contraction of the afferent arteriole for
354 one nephron causes the blood flow to the adjacent nephron to increase. In line with this interpretation, inspection of the
355 arteriolar tree has shown that the nephrons in this case, while sharing an interlobular artery, are too far apart for the
356 vascularly propagated coupling to be active.

357 Fig. 13(a) and (b) show examples of the tubular pressure variations in pairs of neighboring nephrons for hyper-
358 tensive rats. These oscillations are significantly more irregular than the oscillations displayed in Figs. 11 and 12 and, as

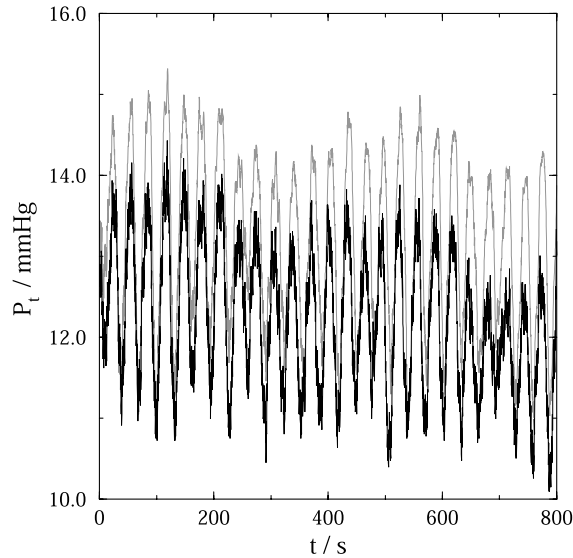


Fig. 11. Tubular pressure variations for a pair of coupled nephrons in a normotensive rat. The pressure variations remain nearly in phase for the entire observation time (or 25 periods of oscillation).

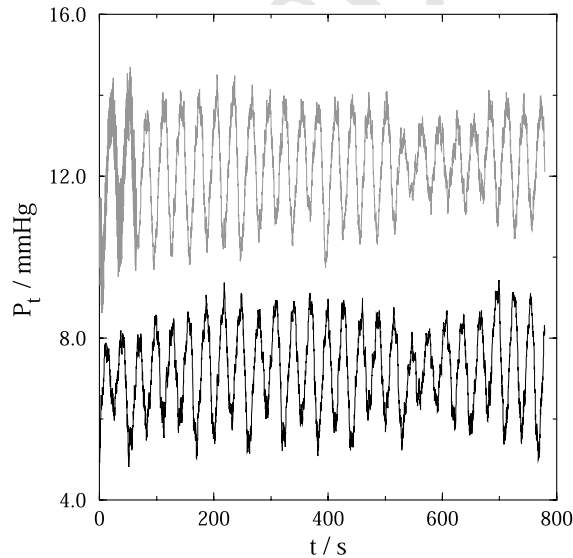


Fig. 12. Anti-phase synchronization in the pressure variations for two neighboring nephrons in a normotensive rat. This type of synchronization is considered to be associated with a strong hemodynamic component in the coupling.

359 previously discussed, it is likely that they can be ascribed to a chaotic dynamics. In spite of this irregularity, however,
360 one can visually observe a certain degree of synchronization between the interacting nephrons. Fig. 14 reproduces the
361 results of a frequency analysis of the two pressure signals in Fig. 13(b). The TGF-mediated oscillations produce the
362 peak at 0.03 Hz, and the arteriolar oscillations show up as a relatively broad peak around 0.2 Hz. One can see how the
363 spectral lines coincide for both the arteriolar oscillations and the TGF mediated oscillations. This implies that these
364 oscillations are synchronized in frequency between the two interacting nephrons.

365 In order to investigate the problem of phase synchronization for the irregular pressure variations in hypertensive rats
366 we have applied the method introduced by Rosenblum and coworkers [37,38]. With this approach one can follow the
367 temporal variation of the difference $\Delta\Phi(t) = \Phi_2(t) - \Phi_1(t)$ between the instantaneous phases $\Phi_1(t)$ and $\Phi_2(t)$ for a pair

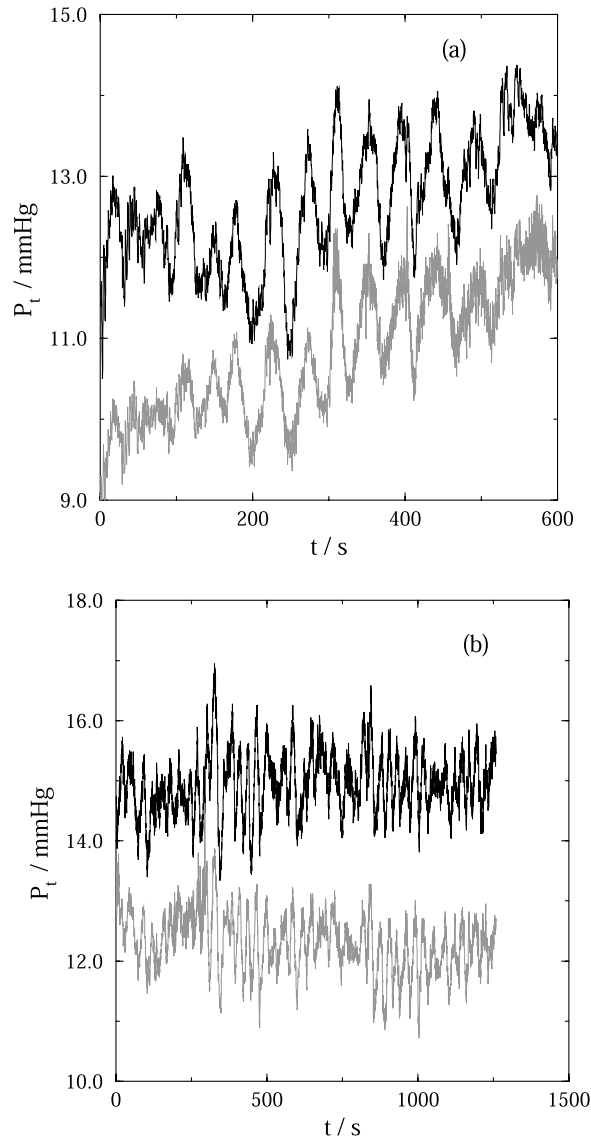


Fig. 13. Two examples (a and b) of the tubular pressure variations that one can observe in adjacent nephrons for hypertensive rats.

368 of coupled chaotic oscillators. The instantaneous phase $\Phi(t)$ and amplitude $A(t)$ for a signal $s(t)$ with complicated
369 (chaotic) dynamics may be defined from

$$A(t)e^{j\Phi(t)} \equiv s(t) + j\tilde{s}(t), \quad (17)$$

371 where

$$\tilde{s}(t) = \frac{1}{\pi} \text{PV} \int_{-\infty}^{\infty} \frac{s(\tau)}{t - \tau} d\tau, \quad (18)$$

373 denotes the Hilbert transform of $s(t)$, j being the imaginary unit. The notation PV implies that the integral should be
374 evaluated in the sense of Cauchy principal value. $m : n$ phase synchronization between two oscillators is said to occur if

$$|n\Phi_2(t) - m\Phi_1(t) - C| < \mu, \quad (19)$$

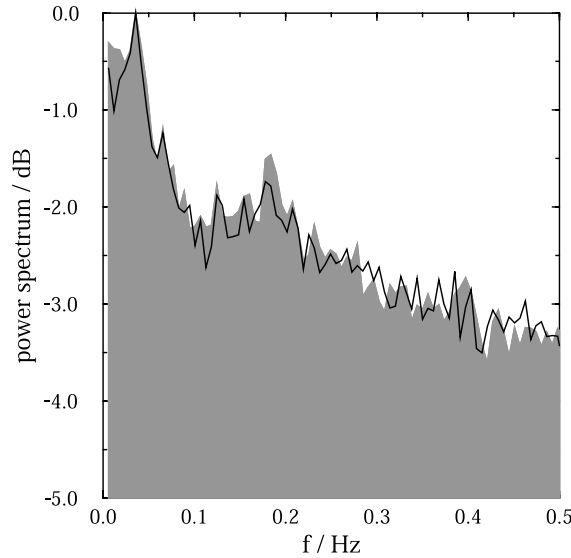


Fig. 14. Spectral distribution of the irregular pressure variations in Fig. 13(b).

376 where μ is a small parameter ($\mu < 2\pi$) that controls the allowed play in the phase locking. In particular, 1:1 phase
 377 synchronization is realized if the phase difference $\Phi_2(t) - \Phi_1(t)$ remains bound to a small interval μ around a mean value
 378 C. For systems subjected to external disturbances or noise one can only expect the condition for phase synchronization
 379 to be satisfied over finite periods of time, interrupted by characteristic jumps in $\Delta\Phi$. Under these circumstances one can
 380 speak about a certain degree of phase synchronization if the periods of phase locking become significant compared to
 381 the characteristic periods of the interacting oscillators [39]. Alternatively, one can use the concept of frequency syn-
 382 chronization if the weaker condition

$$\Delta\Omega = \langle n\dot{\Phi}_2(t) - m\dot{\Phi}_1(t) \rangle = 0 \quad (20)$$

384 is satisfied. Here, $\langle \rangle$ denotes time average, and $\Delta\Omega$ is the difference in (mean) angular frequencies. As noted above, 1:1
 385 frequency synchronization is already distinguishable from the spectral distribution of the experimental data.

386 Fig. 15(a) shows the variation of the normalized phase difference $\Delta\Phi/2\pi$ for the irregular pressure oscillations in Fig.
 387 13(a). One can clearly see the locking intervals with intermediate phase slips. In particular, there is relatively long
 388 interval from $t \cong 160$ to 460 s (corresponding approximately to six oscillations of the individual nephrons) where the
 389 phase difference remains practically constant. Fig. 15(b) reproduces similar results for the irregular pressure variations
 390 in Fig. 13(b). Here, we note the interval from $t \cong 400$ to 600 s (corresponding to eight oscillations of the individual
 391 nephrons) where the phase difference remains nearly constant. We also note that the phase slips typically assume a value
 392 of 2π (or an integer number of 2π -jumps).

393 We conclude that the experimental results show clear evidence of synchronization of neighboring nephrons both for
 394 normotensive and for hypertensive rats. Moreover, one can observe both in-phase and anti-phase synchronization,
 395 associated, presumably, with two different coupling mechanisms between the nephrons. In the next section we shall
 396 study the transitions to and between different regimes of synchronization in the two-nephron model. Particularly in-
 397 teresting in this connection is the role of multistability in the chaotic phase synchronization [40,41].

398 6. Phase multistability

399 Both the above experimental results [17] and our simulations in Section 3 reveal one of the most important features
 400 of the single nephron model, namely the presence of two different time scales in the pressure and flow variations.
 401 Considering the model equations we can identify the two time scales in terms of (i) a low-frequency TGF-mediated
 402 oscillation with a period $T_h \cong 2.2 T$ arising from the delay in the TGF, and (ii) somewhat faster oscillations with a
 403 period $T_v \approx T_h/5$ associated with the adjustment of the arteriolar radius.

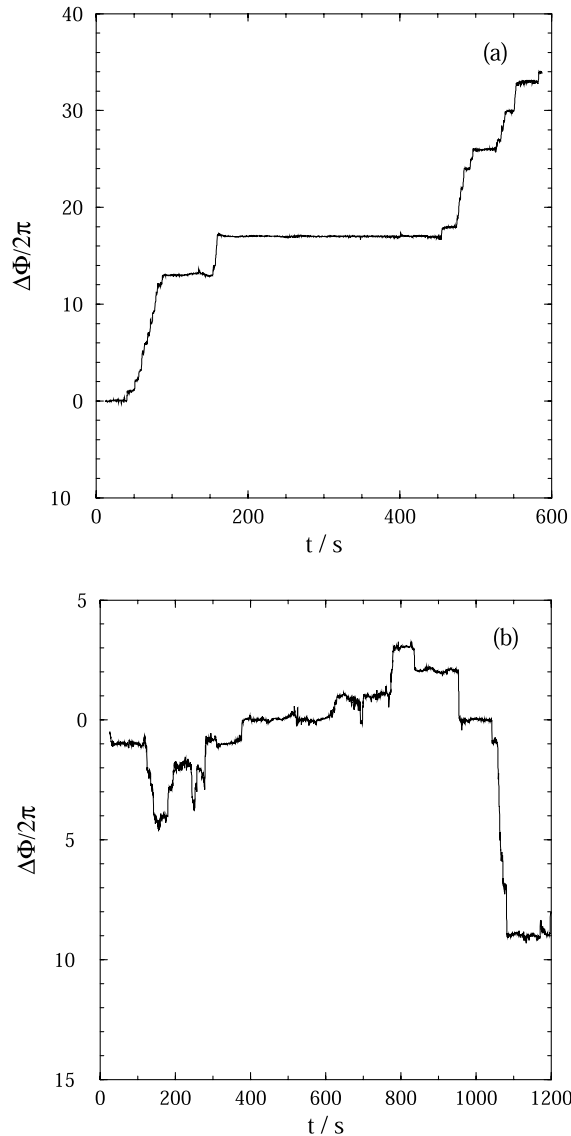


Fig. 15. Variation of the normalized phase difference $\Delta\Phi/2\pi$ for the irregular pressure variations in Fig. 13(a) and (b).

404 To determine T_h and T_v in our numerical simulations we have used the mean return times of the trajectory to
405 appropriately chosen Poincaré sections

$$T_v = \langle T_{\text{ret}}|_{\dot{v}_r=0} \rangle, \quad T_h = \langle T_{\text{ret}}|_{\dot{x}_2=0} \rangle, \quad (21)$$

407 with $\langle \rangle$ denoting the average over many oscillations. As defined in Eq. (10), v_r describes the rate of change for the
408 arteriolar radius.

409 From these return times we can define the intra-nephron rotation number (i.e., the rotation number associated with
410 the two-mode behavior of the individual nephron)

$$\theta_{vh} = T_v/T_h. \quad (22)$$

412 θ_{vh} will be used to characterize the various forms of frequency locking between the two modes.

413 Superimposed onto the two-dimensional bifurcation diagram for the single nephron model as obtained by Andersen
414 et al. [23], Fig. 16 shows the existence of regions with different ratios between the two return times. In the bifurcation

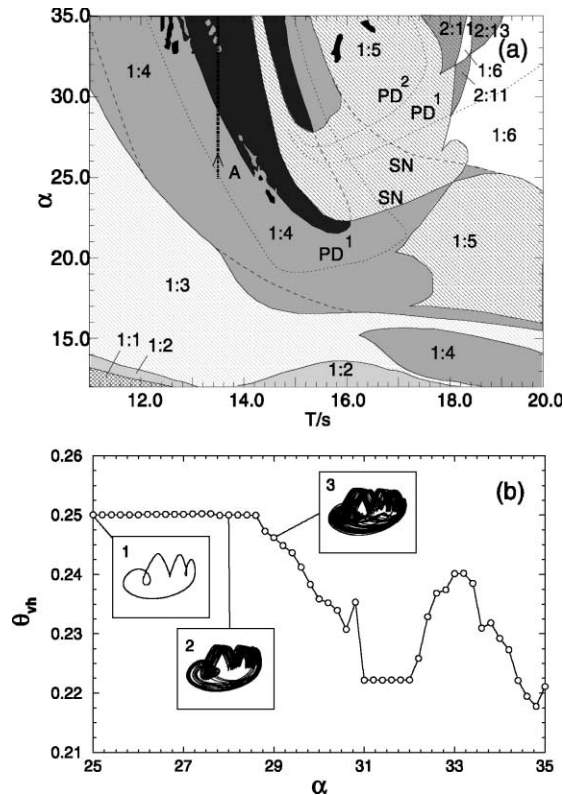


Fig. 16. Two-mode oscillatory behavior in the single nephron model. (a) Rotation number diagram superimposed onto a bifurcation diagram obtained by means of 2D continuation. Dark gray zones represent parameter combinations that lead to chaotic dynamics. Note that in several regions two or more synchronization zones may overlap. (b) The rotation number θ_{vh} as a function of the parameter α along the route A in (a); inserts in (b) show the phase projections on the (P_1, P_2) plane, starting with the 1:4 mode-locked solution.

415 diagram (and in the following discussion) PD denotes a period-doubling bifurcation with the superscript indicating the
 416 period of the solution undergoing the transition, SN denotes a saddle-node bifurcation, and TB a torus birth bifur-
 417 cation (also known as a secondary Hopf bifurcation).

418 With varying feedback delay, Fig. 16(a) shows how the two oscillatory modes can adjust their dynamics so as to
 419 attain different states with rational relations ($n : m$) between the periods. The main (1:1) synchronization regime is
 420 located near $T \cong 2$ s (i.e., outside the figure), but regions of higher resonances (1:4, 1:5, and 1:6) are seen to exist in the
 421 physiologically interesting range of the delay time $T \in [12 \text{ s}, 20 \text{ s}]$.

422 While the transitions between the different locking regimes always involve bifurcations, bifurcations may also occur
 423 within the individual regime. A period-doubling transition, for instance, does not necessarily change θ_{vh} , and the intra-
 424 nephron rotation number may remain constant through a complete period-doubling cascade and into the chaotic re-
 425 gime. This is illustrated in Fig. 16(b) where we have plotted θ_{vh} as a function of the feedback gain α along the route A as
 426 indicated in Fig. 16(a). Phase projections from the various regimes are shown as inserts. Inspection of the figure clearly
 427 shows that θ_{vh} remains constant under the transition from regular 1:4 oscillations (for $\alpha = 25.0$) to chaos (for $\alpha = 28.0$),
 428 see inserts 1 and 2. With further evolution of the chaotic attractor (insert 3), the 1:4 mode locking is destroyed. In the
 429 interval around $\alpha = 31.5$ we observe 2:9 mode locking.

430 We conclude that besides being regular or chaotic, the self-sustained pressure variations in the individual nephron
 431 can be classified as being synchronous or asynchronous with respect to the ratio between the two time scales that
 432 characterize the fast (vascular) mode and the slow (TGF mediated) mode, respectively. This complexity in behavior may
 433 play an essential role in the synchronization between a pair of interacting nephrons. In our investigations we shall
 434 restrict ourselves to consider a parameter range around route A in Fig. 16(a), i.e., $\alpha \in [25, 28]$ and $T \in [12 \text{ s}, 14 \text{ s}]$.

435 Moreover, we shall neglect the hemodynamic coupling ($\varepsilon = 0$) and adopt a more symmetric representation of the
436 vascular coupling, i.e.

$$\psi_{1,2}^* = \psi_{1,2} + \gamma(\psi_{2,1} - \psi_{1,2}) \quad (23)$$

438 instead of the original formulation in Eq. (12).

439 6.1. Symmetrical case $T_1 = T_2$

440 Let us start by examining the bifurcations that occur in a system of two coupled identical nephrons as illustrated in
441 Fig. 17. For $T = 13.5$ s, the individual nephron exhibits stable period-1 dynamics in the entire interval between the Hopf
442 bifurcation at $\alpha \cong 10.5$ and the first period-doubling bifurcation at $\alpha \cong 25.52$. For low coupling strengths and increasing
443 α , the corresponding in-phase solution loses its stability via a pitchfork bifurcation with the formation of two stable
444 symmetrical solutions that each undergoes a cascade of period-doubling bifurcations. The corresponding bifurcational
445 curves are not depicted in Fig. 17. The synchronous anti-phase solution, on the other hand, is stable at low coupling
446 strengths. Time and phase plots for this solution are illustrated in Fig. 18(a) for $\alpha = 26.0$ and $\gamma = 0.01$. The region of
447 anti-phase solution is bounded by the slowly rising (and fully drawn) bifurcation curves TB. These curves extend all the
448 way down to the first period doubling bifurcation for the individual nephron (lower curve) and to the point where the
449 coupled system undergoes a pitchfork bifurcation (upper curve).

450 After the first period-doubling at $\alpha \cong 25.52$, the individual nephron undergoes a series of additional period-dou-
451 blings at $\alpha \cong 26.5, 26.7$, etc. For the in-phase solution I_1 of the coupled-nephron model, the corresponding transitions
452 are delineated by the vertically running lines L^{+1} , PD^2 , and PD^4 . At L^{+1} a stable in-phase period-2 solution arises (in a
453 saddle-node bifurcation for the period-2 solution), and this solution hereafter undergoes a series of period-doubling
454 bifurcations ending in a chaotic regime for $\alpha > 26.7$. Fig. 18(b) shows a couple of time and phase plots for the in-phase
455 period-2 solution observed at $\alpha = 26.0$ and $\gamma = 0.01$. The other (nearly) in-phase period-2 solution I_2 arises in a torus
456 birth bifurcation. In its further development, this solution undergoes a torus bifurcation at the dotted line TB, and I_2
457 hereafter produces (resonant or nonresonant) torus dynamics until it undergoes a transition to chaos via torus
458 breakdown along the curve L_{cr} for large values of α . To the right of this curve we have two stable coexisting chaotic
459 solutions. In one of these solutions, the two nephrons operate in complete synchrony. In the other solution they are
460 synchronized with a small phase lag.

461 So far the picture is similar to prior findings for coupled Rössler oscillators [10,42]. According to these results, the
462 initial Hopf bifurcation for the individual oscillator with the introduction of coupling splits into a Hopf bifurcation

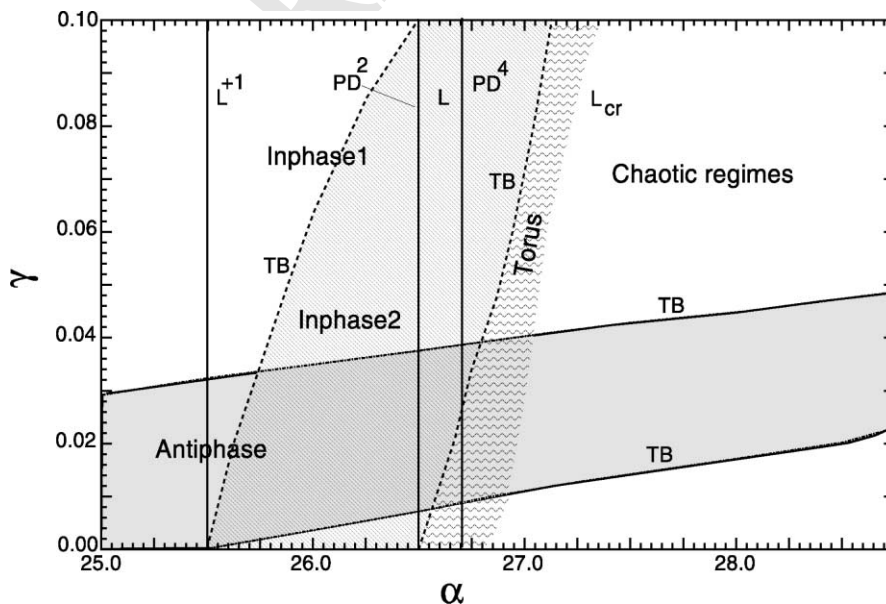


Fig. 17. Simplified two-parameter bifurcation diagram for the coupled nephron model with $T_1 = T_2 = 13.5$ s. γ is the coupling parameter, and α is the feedback strength of the individual nephron.

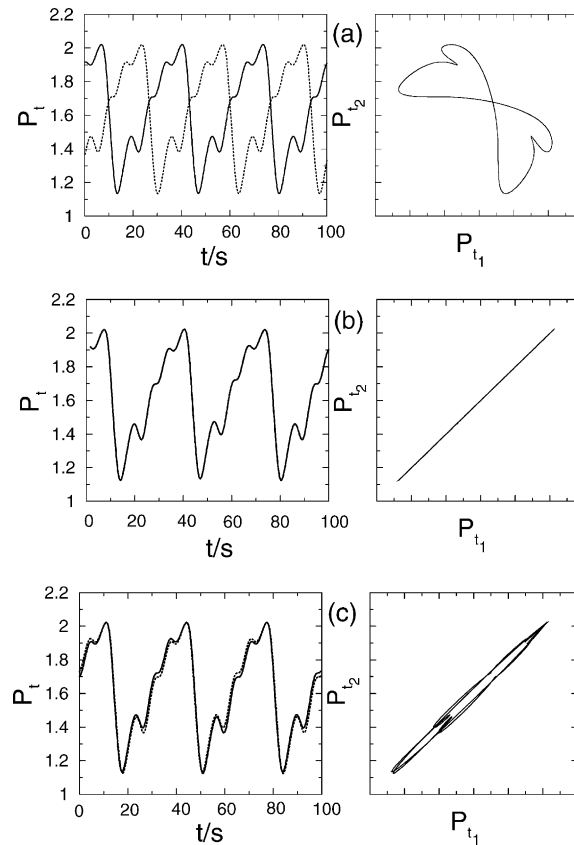


Fig. 18. Coexisting periodic solutions at $\alpha = 26.0$, $\gamma = 0.01$, and $T_1 = T_2 = 13.5$ s. (a) Represents the period-1 anti-phase solution A; (b) and (c) show the two period-2 solutions I_1 and I_2 with phase shifts of 0 and π , respectively, for the subharmonic components.

463 producing a stable anti-phase solution and a Hopf bifurcation producing an unstable in-phase solution. In its further
 464 development, the first period-doubling bifurcation for the individual oscillator is replaced by a torus-birth bifurcation
 465 for the anti-phase solution in the coupled system. The in-phase solution produces a stable period-2 dynamics, which
 466 subsequently undergoes a period-doubling cascade to chaos. After a period-doubling, the nephrons may synchronize in
 467 anti-phase with respect to the subharmonic component. Fig. 18(c) illustrates the time and phase plots for such a so-
 468 lution. This is the solution that we have previously denoted I_2 . Thus for $\alpha = 26.0$, $\gamma = 0.01$ and $T_1 = T_2 = 13.5$ s, the
 469 coupled nephron model displays three coexisting periodic solutions, an anti-phase period-1 solution (Fig. 18(a)), an in-
 470 phase period-2 solution (Fig. 18(b)), and another period-2 solution (Fig. 18(c)) that has a phase shift in the synchron-
 471 ization.

472 However, due to the complicated dynamics of the single nephron model, the coupled system allows for the ap-
 473 pearance of additional solutions via so-called phase multistability [40,41]. The nephrons may synchronize their slow
 474 TGF mediated dynamics with a phase difference corresponding (approximately) to an integer number of periods for the
 475 fast dynamics.

476 6.2. Nonidentical case $T_1 \neq T_2$.

477 Let us hereafter consider how the various dynamical regimes are effected by the introduction of a parameter mis-
 478 match between the functional units. To be concise we shall assume that the feedback delay T_2 for nephron 2 can differ
 479 from the delay $T_1 = 13.5$ s in nephron 1. Fig. 19 shows the regions of stability in the (T_2, γ) parameter plane for each of
 480 the three coexisting periodic solutions in Fig. 18. Inspection of the figure clearly shows that the two period-2 solutions I_1
 481 and I_2 have close, but different stability regions (Arnol'd tongues). Moreover, while the stability region for I_1 is bounded
 482 by lines of saddle-node bifurcations, for I_2 the region is bounded by torus-birth bifurcations. Postnov et al. [40] have

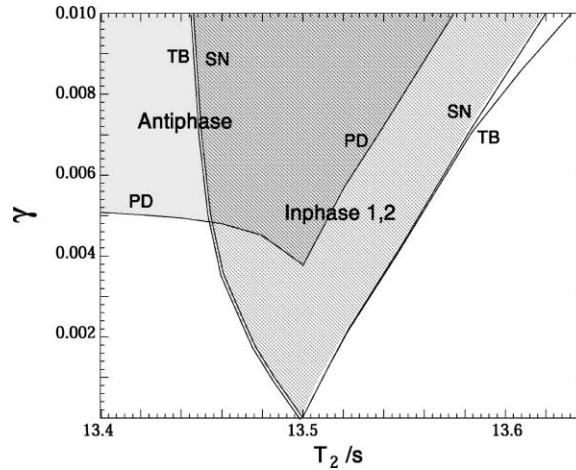


Fig. 19. Synchronization regions for three coexisting types of dynamics at $\alpha = 26.0$ and $T_1 = 13.5$ s. Note the nested character of the synchronization regimes for the two period-2 solutions with different phase shifts for the subharmonic components.

483 previously shown that this type of nested bifurcation structure is characteristic for systems exhibiting multistability
 484 because of the formation of subharmonics. Here, we observe a similar phenomenon for systems with two-mode dy-
 485 namics.

486 The stability region for the anti-phase limit cycle appears not to be the classical resonance horn (Arnol'd tongue) and
 487 does not extend to small values of the coupling strength. It is bounded by period doubling lines PD where a Floquet
 488 multiplier becomes equal to -1 , and the period-1 limit cycle loses its stability. However, no period-2 cycle appears on
 489 these bifurcation lines. We have found that each of the coupled subsystems is responsible for one PD line. For the
 490 symmetrical case $T_1 = T_2 = 13.5$ s, both bifurcations take place simultaneously, and the transition is diagnosed as a
 491 torus-birth bifurcation.

492 In the considered parameter range, three coexisting synchronous solutions are detected. Two of the solutions define
 493 different families arising in the first period-doubling bifurcation for the individual system, and more complicated so-
 494 lutions may develop from these for larger α . The third mode is an anti-phase solution which only arises at finite coupling
 495 strengths.

496 Analyses of self-modulated oscillations with $1 : m$ ratios of the periods show that the phase difference can attain m
 497 different values [43]. Since the single nephron operates in $1:4$ self-modulated regime, four phase shifted solutions coexist
 498 in the coupled system. In this case, the phase difference attains different values (Fig. 20(a)), and the solutions lose
 499 stability one by one as the parameter mismatch is increased (Fig. 20(b)).

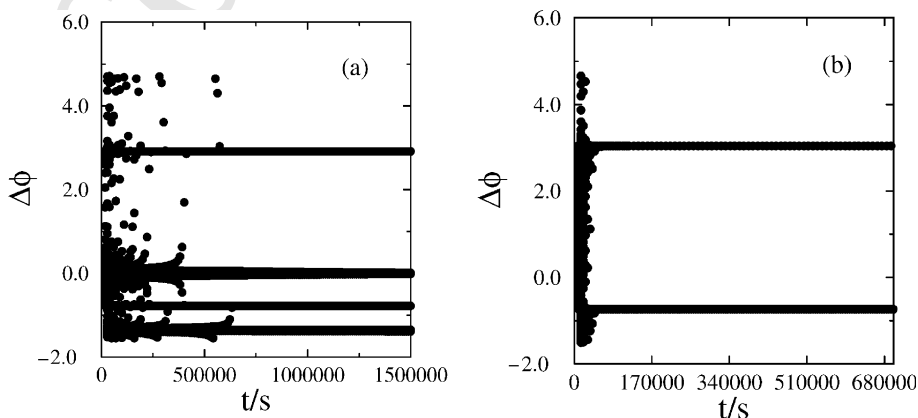


Fig. 20. The phase difference approaches (a) four stationary values for identical systems ($T_1 = T_2 = 16.0$ s) but only (b) two values when a mismatch is introduced ($T_1 = 15.99375$ s, $T_2 = 16.0$ s). α is fixed at 18.595.

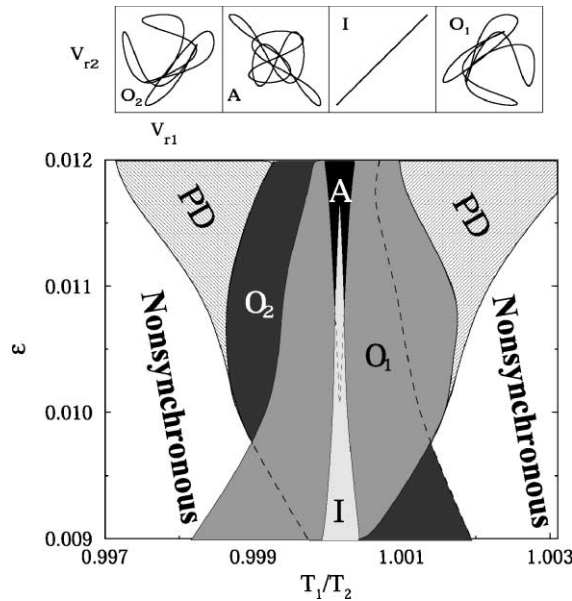


Fig. 21. Synchronization regions for coexisting families of attractors ($\alpha = 18.595$, $T_2 = 16.0$ s, $\gamma = 0.004$). In-phase ($\Delta\phi = 0.0$) and anti-phase ($\Delta\phi = -1.3474$) solutions are labeled I and A, respectively. Two out-of-phase regimes with $\Delta\phi = -0.7773$ and 2.9129 are indicated as O_1 and O_2 . PD denotes regions of period-doubled solutions. The inserts show characteristic phase space projections of the four synchronized solutions. The projection plane is spanned by the rates $v_r = \dot{r}$ for each of the two nephrons.

500 Fig. 21 shows a segment of the bifurcation diagram for synchronous solutions on the mismatch vs. hemodynamic
 501 coupling parameter plane. The strength of the vascularly propagated interaction is fixed at 0.004. In-phase oscillations
 502 are stable when both interacting systems are nearly identical ($T_1 \approx T_2$) and the hemodynamic coupling is weak enough
 503 ($\varepsilon < 0.0115$). However, due to the self-modulated nature of the oscillations in the individual nephron, there are also two
 504 stable out-of-phase synchronous regimes (O_1 and O_2). When ε increases, the antiphase regime A also becomes stable
 505 due to the effect of the hemodynamic coupling. Within some interval of ε , there are four stable coexisting solutions: the
 506 in-phase solution I, the anti-phase solution A, and two out-of-phase regimes O_1 and O_2 inspection of the figure clearly
 507 shows that the synchronization region has a complicated inherent structure. With increasing mismatch, the O_1 and O_2
 508 cycles lose their stability via a tangent bifurcation (entering the nonsynchronous region) or via a period doubling at the
 509 border of the PD zone in Fig. 21.

510 7. Transition to synchronous chaotic behavior

511 For weakly developed chaos the features of chaotic phase synchronization have been investigated in significant detail
 512 using three dimensional models of chaotic oscillations [37,38]. However, our problem differs from previously studied
 513 cases because the individual oscillatory system has two modes that can be locked with each other. As we shall see, an
 514 interaction between the subsystems can break their mutual adjustment. It is also possible that the coupling can act in a
 515 different manner on the fast and slow oscillations. It is of interest to know to what extent the oscillatory modes adjust
 516 their motions in accordance to one another when the coupling is introduced. For the interacting nephrons we introduce
 517 two rotation numbers as follows:

$$\theta_v = T_{v1}/T_{v2}, \quad \theta_h = T_{h1}/T_{h2}. \quad (24)$$

519 To provide more information, the variation of the phase difference is calculated separately for the slow and for the fast
 520 oscillations.

521 Let us consider the case of $\alpha = 27.30$ corresponding to a weakly developed chaotic attractor in the individual
 522 nephron. The coupling strength γ and delay time T_2 in the second nephron are varied. The obtained results are

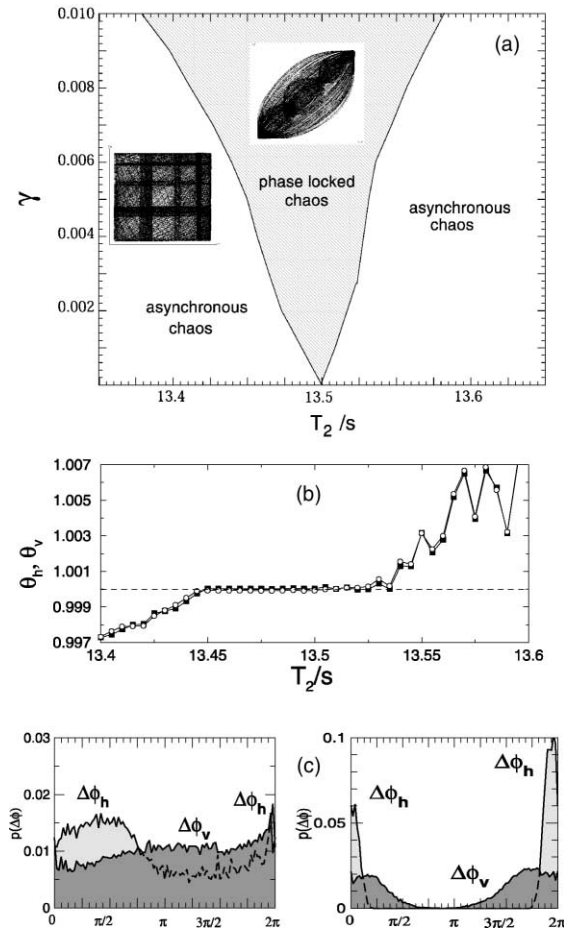


Fig. 22. Chaotic phase synchronization at $\alpha = 27.30$. (a) Diagram of synchronous and asynchronous chaotic behavior with the corresponding (P_1, P_2) phase projections (in inserts); (b) the rotation numbers θ_h (\circ) and θ_v (\blacksquare) vs. T_2 ; (c) distribution of the phase difference for $\gamma = 0.006$ for asynchronous chaos (left) at $T_2 = 13.4$ s and for synchronous chaos (right) at $T_2 = 13.5$ s.

523 summarized in Fig. 22. Two distinct chaotic states can be detected and classified, respectively, as asynchronous and
 524 synchronous chaos. Outside the synchronization region, the phase projection has a square shape (Fig. 22(a)). Both θ_h
 525 and θ_v change continuously with T_2 (Fig. 22(b)), and the phase difference appears to be nearly uniformly distributed
 526 over the interval $[0, 2\pi]$ for both time scales (Fig. 22(c)).

527 Inside the synchronization region the projection of the phase trajectory, while remaining chaotic, changes its shape
 528 to become more aligned with the main diagonal (Fig. 22(a)). The rotation numbers θ_h and θ_v in this case are both equal
 529 to unity in every point of the synchronization area (Fig. 22(b)). For both time scales there is a finite interval (located to
 530 around π) of phase differences whose numerically calculated probability is equal to zero (Fig. 22(c)). Thus, the phase
 531 difference for the synchronous chaotic oscillation is concentrated within a certain interval. This defines chaotic phase
 532 synchronization in the sense of Pikovsky and Rosenblum [37,38].

533 The crosshatched triangular zone on the (T_2, γ) parameter plane in Fig. 22(a) represents the region of stability for the
 534 synchronous chaotic attractor. Like the synchronization region for the periodic oscillations, it becomes wider with
 535 increasing coupling strength. Note that there are no qualitative difference in the dynamics of the slow and fast time
 536 scales. They both become synchronized at the same values of the control parameters. In this range of parameters the
 537 coupled two-mode chaotic oscillators operate as one-mode chaotic oscillators like two coupled Rössler systems [37,41].
 538 However, the two-mode oscillations demonstrate more complex behavior for other values of the control parameters.

539 With increasing α (moving to the right part of Fig. 17) the synchronized chaotic regime described in the previous
 540 section is destroyed. However, other transitions to chaotic synchronization can be found. The most interesting one,

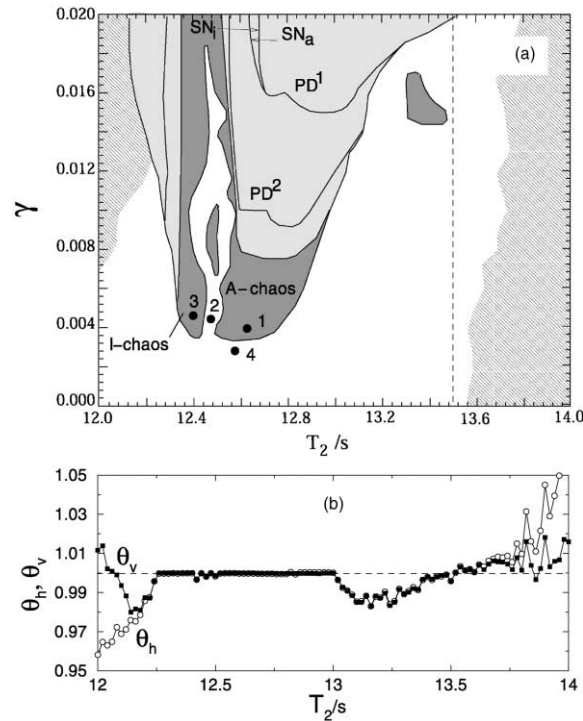


Fig. 23. Chaotic phase synchronization at $\alpha = 28.0$: Transition from anti-phase to in-phase solutions. (a) Diagram of the main dynamical regimes; (b) rotation numbers θ_h (\circ) and θ_v (\blacksquare) as functions of T_2 at $\gamma = 0.01$.

541 occurring at $\alpha \approx 28.0$, is related to the bifurcations of the anti-phase family which originates from the limit cycle in Fig.
542 18(a).

543 Fig. 23 shows a diagram of the dynamical regimes. For the symmetric case $T_1 = T_2 = 13.5$ s (dashed line in Fig. 23),
544 the period-one anti-phase limit cycle loses its stability when the coupling is decreased. However, for $T_2 < 13.5$ s there is
545 a range of α where the anti-phase solutions undergo a number of bifurcations while maintaining synchrony. A reduction
546 of the coupling strength γ for $T_2 \in [12.6 \text{ s}; 12.8 \text{ s}]$ leads to a period-doubling cascade and to the formation of an
547 anti-phase chaotic regime (“A-chaos” zone in Fig. 23(a)).

548 The anti-phase solution can lose its stability in two different ways:

549 (i) Increasing T_2 produces a transition from synchronous to asynchronous chaos (panels 1 and 4 in Fig. 24) similar to
550 the transition for the in-phase solution described in the previous section;

551 (ii) Decreasing T_2 leads to a transition between the regimes of anti-phase and in-phase chaotic synchronization.

552 Let us consider the latter transition in more detail. Fig. 23(b) displays the rotation numbers θ_h and θ_v plotted against
553 T_2 for $\gamma = 0.01$. Besides the synchronous regime where both θ_h and θ_v are equal to unity, we note that two different
554 types of asynchronous behavior can be detected. For one of these $\theta_h = \theta_v$, as it was demonstrated in the previous
555 section. For $T_2 < 12.2$, however, another type of asynchronous behavior arises which is characterized by the condition
556 $\theta_h \neq \theta_v$. This means that the rotation numbers θ_{vh1} and θ_{vh2} take different values in the interacting nephron models, i.e.,
557 the resonance relation between slow and fast oscillations is broken. Thus, the vascularly propagated coupling can lead
558 to desynchronization of oscillations in coupled nephrons, and it can also break the entrainment of the time scales in
559 each subsystem.

560 The plateau in Fig. 23(b) for $T_2 \in [12.25 \text{ s}; 13.0 \text{ s}]$ indicates the presence of synchronous oscillations in the two
561 nephrons. However, the different parts of this interval correspond to different oscillatory regimes. Namely, with varying
562 T_2 the anti-phase chaotic attractor (panel 1 in Fig. 24) transforms into an in-phase attractor at $T_2 \approx 12.5$ s (panel 3 in
563 Fig. 24). In panel 2 of Fig. 24 one clearly sees the intermediate state of desynchronization when the chaotic regime
564 continuously drifts over different phase relations, sharing the signs of both in-phase and anti-phase regimes. Thus the
565 appearance of anti-phase synchronization and the transition to the in-phase regime are related to the vascularly
566 propagated coupling that influences the fast and slow oscillatory modes in different ways.

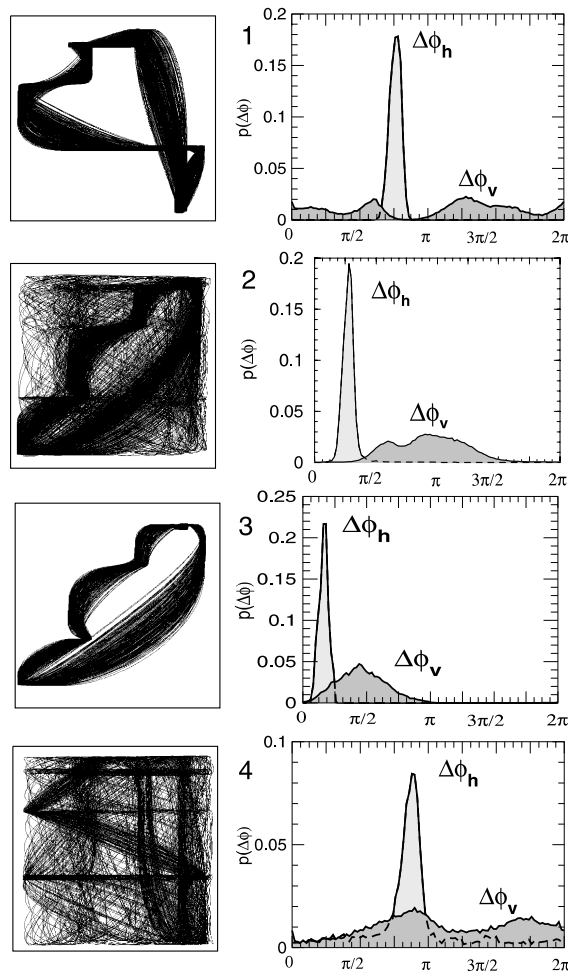


Fig. 24. Chaotic phase synchronization at $\alpha = 28.0$: The phase projections (P_{11}, P_{12}) and the distribution of the phase difference at the points marked in Fig. 23(a).

567 Since we investigate a two-mode self-sustained oscillator, the following question arises: Is it possible to reach a state
568 of partial phase synchronization where only one of the modes is synchronized? We suppose that desynchronization can
569 take place either through varying nonlinearity or via increased mismatch parameter. Let us consider the two cases
570 separately.

571 7.1. Identical case $T_1 = T_2$

572 Fig. 25 presents the phase distribution of the fast and slow oscillations. The distributions in Fig. 25(a) are clearly in
573 accordance with the definition of phase synchronization for chaotic oscillations. The distribution functions are bounded
574 and localized in the vicinity of some average value around 0 (and 2π). With increasing nonlinearity parameter α , the
575 phase difference for the slow oscillations $\Delta\phi_h$ maintains the the same distribution while the phase distribution of the fast
576 oscillations $\Delta\phi_v$ indicates the destruction of phase synchronization. Thus, with increasing α , the two internal time scales
577 demonstrate different phase coherence properties. Note, however, that the nephrons remain frequency locked (insert 2
578 in Fig. 16(b)) because of the homogeneity of the interacting functional units. We conclude that a regime classified as
579 partial phase synchronization of chaotic two-mode oscillations can be observed.

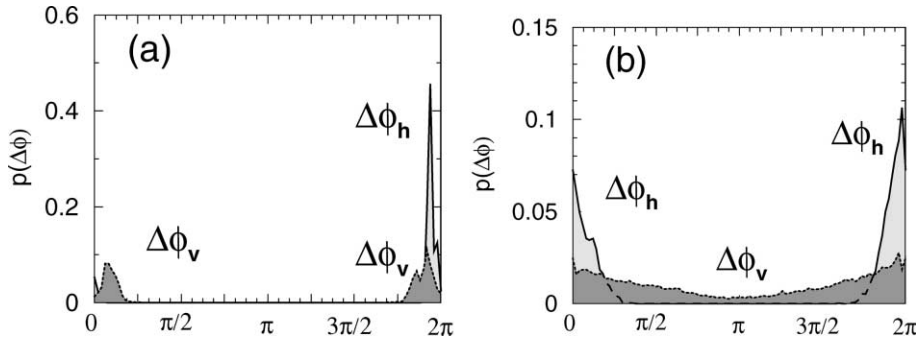


Fig. 25. Partial phase desynchronization when α changes from 27.2 (a) to 28.0 (b) at $\gamma = 0.06$. Both the fast and the slow mode remain frequency locked, but the phase synchronization of the fast mode is lost.

580 7.2. Nonidentical case $T_1 \neq T_2$

581 To investigate the degree of frequency and phase entrainments we change T_2 while $T_1 = 13.5$ s. Plots of the rotation
582 numbers θ_h and θ_v with varying T_2 illustrate a number of remarkable results (Fig. 26): while the slow h-mode of chaotic
583 oscillations remain locked within a wide range of T_2 , the fast v-mode behaves in a complicated way assuming resonant
584 values at particular values of T_2 .

585 Even with a small mismatch we can not diagnose frequency (phase) synchronization of the v-mode for coupled
586 nephrons whose frequencies coincide only for a certain value of T_2 . Being almost uniformly distributed over the interval
587 $[0, 2\pi]$, the phase difference for the v-mode drifts in time even in the symmetrical case Fig. 26(b) and with increasing
588 mismatch it finally decreases monotonically. In this way our numerical simulations reveal the existence of parameter

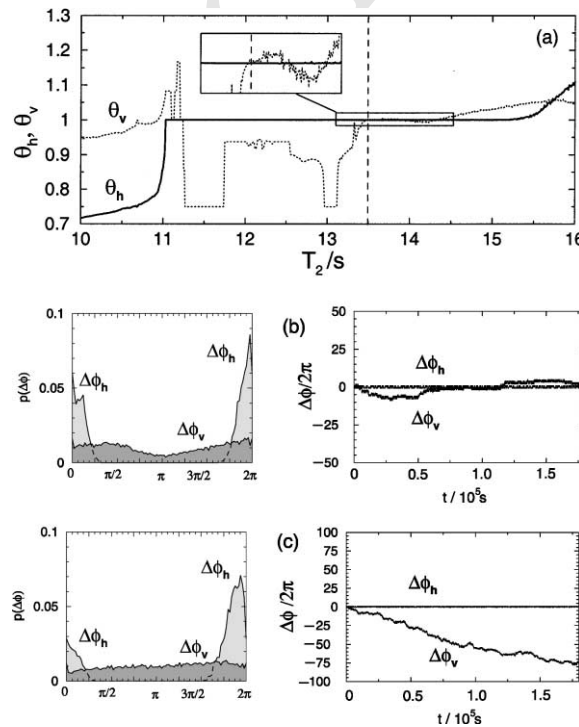


Fig. 26. Transition from partial phase synchronization to partial frequency synchronization at $\alpha = 29.0$ and $\gamma = 0.06$. (a) Variation of T_2 reveals the different behaviors of θ_h and θ_v ; (b) oscillations are desynchronized with respect to their phases but the average frequency difference is still zero ($T_1 = T_2 = 13.5$ s); (c) both the phase and the frequency difference manifest asynchronous behavior with respect to the v-oscillations while the h-oscillations remain synchronous ($T_2 = 13.71$ s).

589 ranges (i) with partial synchronization where the synchronization conditions are fulfilled only for one of the oscillatory
590 modes and (ii) with frequency but no phase entrainments.

591 8. Conclusion

592 In this paper we have considered a fully deterministic description both of the function of individual nephron and of
593 the nephron–nephron interaction. With physiologically realistic mechanisms and with independently determined pa-
594 rameters this has allowed us to explain how the pressure and flow regulation in the nephron becomes unstable in a Hopf
595 bifurcation and how more complicated dynamics can arise as the feedback gain is increased. For coupled nephrons we
596 have been able to explain both the observation of in-phase and anti-phase synchronization in the pressure variations for
597 neighboring nephrons in normotensive rats and of chaotic phase synchronization in hypertensive rats. The various
598 synchronization phenomena are likely to have significant physiological ramifications, and transitions between different
599 states of synchronization may play an important role in the regulation of the kidney. In-phase synchronization, for
600 instance, in which the nephrons simultaneously perform the same regulatory adjustments of the incoming blood flow, is
601 likely to produce synergetic effects in the overall response of the system to external disturbances. Out-of-phase syn-
602 chronization, on the other hand, will produce a slower and less pronounced response of the nephron system in the
603 aggregate.

604 In practice the nephrons exist and operate in a very noisy environment. The influence of noise is partly illustrated in
605 Fig. 15 where the chaotic phase synchronization is interrupted by phase jumps where the synchronization is momen-
606 tarily lost. Noise is also expected to wash out many of details in our bifurcation diagrams, and further investigations
607 obviously have to consider this phenomenon in detail.

608 Another problem of considerable interest concerns the range of the synchronization between the nephrons. Since the
609 arteriolar network can be mapped out and the length and diameters of various vessels determined, it is possible to
610 obtain an independent estimate of the typical strength of the hemodynamic coupling and its variation across the kidney.
611 Similarly, determination of the decay length for the vascularly propagated signal will allow us to estimate the pa-
612 rameters of that coupling. The typical length of the vascular segments separating neighboring glomeruli is of the order
613 of 250–300 μm . This is only about 30% of the distance that the vascular signal is expected to propagate, suggesting that
614 larger groups of nephrons might act in synchrony. We are presently trying to establish an experimental procedure that
615 will allow us to study the more global effects of the nephron–nephron interaction.

616 9. Uncited reference

617 [29]

618 Acknowledgements

619 This work was partly supported by CRDF grant (REC-006) and RFBR (01-02-16709). OS acknowledges Natural
620 Science Foundation of Denmark and INTAS grant (YSF 01/1-0023).

621 References

- 622 [1] Moore LC. Tubuloglomerular feedback and SNGFR autoregulation in the rat. *Am J Physiol* 1984;247:F267–76.
623 [2] Leyssac PP, Baumbach L. An oscillating intratubular pressure response to alterations in Henle loop flow in the rat kidney. *Acta*
624 *Physiol Scand* 1983;117:415–9.
625 [3] Holstein-Rathlou N-H, Leyssac PP. TGF-mediated oscillations in the proximal intratubular pressure: differences between
626 spontaneously hypertensive rats and wistar-kyoto rats. *Acta Physiol Scand* 1986;126:333–9.
627 [4] Leyssac PP, Holstein-Rathlou N-H. Effects of various transport inhibitors on oscillating TGF pressure response in the rat.
628 *Pflügers Archiv* 1986;407:285–91.
629 [5] Holstein-Rathlou N-H, Marsh DJ. Renal blood flow regulation and arterial pressure fluctuations: a case study in nonlinear
630 dynamics. *Physiol Rev* 1994;74:637–81.
631 [6] Yip K-P, Holstein-Rathlou N-H, Marsh DJ. Chaos in blood flow control in genetic and renovascular hypertensive rats. *Am J*
632 *Physiol* 1991;261:F400–8.
633 [7] Yip K-P, Holstein-Rathlou N-H. Chaos and non-linear phenomena in renal vascular control. *Cardiovasc Res* 1996;31:359–70.

- 634 [8] Jensen KS, Holstein-Rathlou N-H, Leyssac PP, Mosekilde E, Rasmussen DR. Chaos in a system of interacting nephrons. In:
635 Degn H, Holden AV, Olsen LF, editors. Chaos in Biological Systems. New York: Plenum; 1987. p. 23–32.
- 636 [9] Jensen KS, Mosekilde E, Holstein-Rathlou N-H. Self-sustained oscillations and chaotic behaviour in kidney pressure regulation.
637 *Mondes en Develop* 1986;54/55:91–109.
- 638 [10] Mosekilde E. Topics in nonlinear dynamics. Applications to physics, biology and economic systems. Singapore: World Scientific;
639 1996.
- 640 [11] Briggs J. A simple steady-state model for feedback control of glomerular filtration rate. *Kidney Int* 1982;22(Suppl. 12):S143–50.
- 641 [12] Leyssac PP, Holstein-Rathlou N-H. Tubulo-glomerular feedback response: enhancement in adult spontaneously hypertensive rats
642 and effects of anaesthetics. *Pflügers Archiv* 1989;413:267–72.
- 643 [13] Holstein-Rathlou N-H, Marsh DJ. A dynamic model of the tubuloglomerular feedback mechanism. *Am J Physiol*
644 1990;258:F1448–59.
- 645 [14] Holstein-Rathlou N-H, Marsh DJ. Oscillations of tubular pressure, flow, and distal chloride concentration in rats. *Am J Physiol*
646 1989;256:F1007–14.
- 647 [15] Layton HE, Pitman EB, Moore LC. Bifurcation analysis of TGF-Mediated Oscillations in SNGFR. *Am J Physiol* 1991;261:F904–
648 19.
- 649 [16] Hollenberg NK, Sandor T. Vasomotion of renal blood flow in essential hypertension. Oscillations in xenon transit. *Hypertension*
650 1984;6:579–85.
- 651 [17] Holstein-Rathlou N-H, Wagner AJ, Marsh DJ. Tubuloglomerular feedback dynamics and renal blood flow autoregulation in rats.
652 *Am J Physiol* 1991;260:F53–68.
- 653 [18] Feldberg R, Colding-Jørgensen M, Holstein-Rathlou N-H. Analysis of interaction between TGF and the myogenic response in
654 renal blood flow autoregulation. *Am J Physiol* 1995;269:F581–93.
- 655 [19] Casellas D, Dupont M, Bouriquet N, Moore LC, Artuso A, Mimran A. Anatomic pairing of afferent arterioles and renin cell
656 distribution in rat kidneys. *Am J Physiol* 1994;267:F931–6.
- 657 [20] Holstein-Rathlou N-H. Synchronization of proximal intratubular pressure oscillations: evidence for interaction between
658 nephrons. *Pflügers Archiv* 1987;408:438–43.
- 659 [21] Bohr H, Jensen KS, Petersen T, Rathjen B, Mosekilde E, Holstein-Rathlou N-H. Parallel computer simulation of nearest-
660 neighbour interaction in a system of nephrons. *Parallel Comp* 1989;12:113–20.
- 661 [22] Barfred M, Mosekilde E, Holstein-Rathlou N-H. Bifurcation analysis of nephron pressure and flow regulation. *Chaos* 1996;6:280–
662 7.
- 663 [23] Andersen MD, Carlsson N, Mosekilde E, Holstein-Rathlou N-H. Dynamic model of nephron–nephron interaction. In: Layton H,
664 Weinstein A, editors. Membrane Transport and Renal Physiology. New York: Springer-Verlag; 2002.
- 665 [24] Holstein-Rathlou N-H, Yip K-P, Sosnovtseva OV, Mosekilde E. Synchronization phenomena in nephron–nephron interaction.
666 *Chaos* 2001;11:417–26.
- 667 [25] Postnov DE, Sosnovtseva OV, Mosekilde E, Holstein-Rathlou N-H. Cooperative phase dynamics in coupled nephrons. *Int J Mod*
668 *Phys B* 2001;15:3079–98.
- 669 [26] Holstein-Rathlou N-H, Leyssac PP. Oscillations in the proximal intratubular pressure: a mathematical model. *Am J Physiol*
670 1987;252:F560–72.
- 671 [27] Deen WM, Robertson CR, Brenner BM. A model of glomerular ultrafiltration in the rat. *Am J Physiol* 1984;223:1178–83.
- 672 [28] Rosenbaum M, Race D. Frequency-response characteristics of vascular resistance vessels. *Am J Physiol* 1968;215:1397–402.
- 673 [29] Fung Y-CB. Biomechanics. Mechanical properties of living tissues. New York: Springer; 1981.
- 674 [30] Parker TS, Chua LO. Practical numerical algorithms for chaotic systems. Berlin: Springer-Verlag; 1989.
- 675 [31] Marek M, Schreiber I. Chaotic behavior in deterministic dissipative systems. England: Cambridge University Press; 1991.
- 676 [32] Wolf A. Quantifying chaos with lyapunov exponents. In: Holden AV, editor. Chaos. England: Manchester University Press; 1986.
- 677 [33] Chen Y-M, Yip K-P, Marsh DJ, Holstein-Rathlou N-H. Magnitude of TGF-initiated nephron–nephron interactions is increased
678 in SHR. *Am J Physiol* 1995;269:F198–204.
- 679 [34] Arnol'd VI. Small denominators. I. Mapping of the circumference onto itself. *Am Math Soc Transl Ser 2* 1965;46:213–84.
- 680 [35] Yip K-P, Holstein-Rathlou N-H, Marsh DJ. Dynamics of TGF-initiated nephron–nephron interactions in normotensive rats and
681 SHR. *Am J Physiol* 1992;262:F980–8.
- 682 [36] Källskog Ö, Marsh DJ. TGF-initiated vascular interactions between adjacent nephrons in the rat kidney. *Am J Physiol*
683 1990;259:F60–4.
- 684 [37] Rosenblum MG, Pikovsky AS, Kurths J. Phase synchronization of chaotic oscillators. *Phys Rev Lett* 1996;76:1804–7.
- 685 [38] Pikovsky AS, Rosenblum MG, Osipov GV, Kurths J. Phase synchronization of chaotic oscillators by external driving. *Physica D*
686 1997;104:219–38.
- 687 [39] Stratonovich LR. Topics in the theory of random noise. New York: Gordon and Breach; 1963.
- 688 [40] Postnov DE, Vadivasova TE, Sosnovtseva OV, Balanov AG, Anishchenko VS, Mosekilde E. Role of multistability in the
689 transition to chaotic phase synchronization. *Chaos* 1999;9:227–32.
- 690 [41] Vadivasova TE, Sosnovtseva OV, Balanov AG, Astakhov VV. Phase multistability of synchronous chaotic oscillations. *Discrete*
691 *Dyn Nat Soc* 2000;4:231–43.
- 692 [42] Rasmussen J, Mosekilde E, Reick Chr. Bifurcations in two coupled Rössler systems. *Math Comp Sim* 1996;40:247–70.
- 693 [43] Sosnovtseva OV, Postnov DE, Nekrasov AM, Mosekilde E. Phase multistability analysis of self-modulated oscillations. *Phys.*
694 *Rev. E* submitted for publication.